

# Structure Regulation and Energy Storage Mechanisms of Bismuth-Based Anodes for Sodium Ion Batteries

Lina Zhao<sup>+[a]</sup> Yuhao Wen<sup>+[a]</sup> Shangyi Bi,<sup>[a]</sup> Junyi Li,<sup>[a]</sup> Hongjian Zhang,<sup>[a]</sup> Li Liu,<sup>[a]</sup> Fanian Shi,<sup>[a]</sup> Jie Yan,<sup>+[b]</sup> Shanshan Pan,<sup>[c]</sup> and Haitao Zhang\*<sup>+[b]</sup>

The increasing demand for eco-friendly energy storage solutions has driven significant interest in sodium-ion batteries (SIBs) as an alternative to lithium-ion batteries, primarily due to sodium's abundant availability. Among various anode materials, bismuth (Bi) has emerged as a promising candidate due to its high theoretical volumetric capacity and excellent electrical conductivity. This review presents a comprehensive analysis of structural characteristics and failure mechanisms inherent to Bi-based anode materials for SIBs, providing valuable insights into the significance of material modification methods. Structure regulation strategies for Bi-based SIB anodes are reviewed,

focusing on the challenges associated with volumetric expansion and strategies to enhance their electrochemical performance. Typically, nanostructure optimization, surface engineering, morphology modification, and composition regulation are highlighted. Furthermore, this review will discuss the underlying mechanisms that improve sodium storage capabilities and the role of bismuth in advancing the efficiency and stability of SIBs. Lastly, the prospects and imminent challenges associated with bismuth-based materials will be presented, providing insights for future research and development in energy storage technologies.

## 1. Introduction

With the energy structure transition of contemporary society and the increasing concerns about environmental pollution, new eco-friendly renewable energy storage technologies have been widely proposed to optimize energy utilization and to enhance the efficiency of energy production.<sup>[1–5]</sup> The rapid emergence of the renewable energy sectors has highlighted the limitations of traditional batteries, which have quickly lost their competitiveness due to high costs and short life spans. In contrast, rechargeable batteries have demonstrated substantial capacity and long cycle life and have significantly advanced the potential of the new energy industry.<sup>[6–10]</sup> To seize the opportunities presented by these advancements, lithium-ion batteries (LIBs) have been instrumental for decades. However, the global lithium reserves are geographically limited. Sodium, sharing similar physicochemical properties with lithium belongs to the same main group, is far more abundant on Earth. Consequently, there is a growing interest among researchers in exploring sodium-ion batteries (SIBs) as a partial substitute for LIBs.

It is well-established that the standard redox potential of  $\text{Na}^+/\text{Na}$  ( $-2.71\text{ V}$ ) relative to the standard hydrogen electrode is higher to that of  $\text{Li}^+/\text{Li}$  ( $-3.04\text{ V}$ ). Furthermore, sodium atom has a larger ionic radius ( $1.02\text{ \AA}$ ) compared to lithium ( $0.76\text{ \AA}$ ).<sup>[11–13]</sup> These differences in redox potential and size mean that certain materials that function effectively in LIB electrodes may not deliver competitive energy density when used in SIBs. Additionally, the electrode materials in SIBs (especially anode materials) must accommodate a greater volume expansion during the repeated Na ion insertion/desertion process compared to LIBs. To address these challenges, researchers have developed various materials that are more effective for sodium ion storage.

For anode materials for SIBs, three fundamental electrochemical storage mechanisms have been identified: intercalation, conversion, and alloying.<sup>[8]</sup> Intercalation-type materials, such as graphite—a traditional anode material for LIBs successfully commercialized decades ago—experience significant stress during the  $\text{Na}^+$  intercalation and deintercalation processes. Additionally, the Na-graphite compounds are thermodynamically unstable.<sup>[11,13,14]</sup> As a result, hard carbon has emerged as an alternative for SIBs. Beyond intercalation-type materials, other anode options also face challenges due to volume expansion issue for  $\text{Na}^+$  storage. Conversion-type materials can achieve high specific capacities through cation conversion reactions; however, their low electrical conductivity and slow kinetic behavior often inhibit their long-life cycling performance and rate capability.<sup>[15–17]</sup> Similarly, alloy-type anodes can provide higher capacities by forming sodium alloys, but they are prone to more significant volume expansion during electrochemical processes. Elements such as phosphorus (P), tin (Sn), antimony (Sb), germanium (Ge), and bismuth (Bi) are primarily selected by researchers to synthesize alloy-type anodes.<sup>[18–22]</sup> The illustration

[a] L. Zhao,<sup>+</sup> Y. Wen,<sup>+</sup> S. Bi, J. Li, H. Zhang, L. Liu, F. Shi

Key Laboratory of Polymer and Catalyst Synthesis Technology of Liaoning Province, School of Environmental and Chemical Engineering, Shenyang University of Technology, Shenyang 110870, China

[b] J. Yan, H. Zhang

Beijing Key Laboratory of Ionic Liquids Clean Process, Institute of Process Engineering, Chinese Academy of Sciences, Beijing 100190, China  
E-mail: htzhang@ipe.ac.cn

[c] S. Pan

School of Energy Science and Technology, Henan University, Zhengzhou 450046, China

[+] Lina Zhao and Yuhao Wen contribute equally to this work.

of three fundamental electrochemical storage mechanisms is present in Figure 1.

## 2. Characteristics and Challenges of Bismuth-Based Anode Materials

Bismuth (Bi), as the heaviest naturally occurring member of the pnictogen family (Group 15, also known as VA Family, including N, P, As, Sb, Bi), has emerged as promising candidate for anodes in energy storage systems due to their environmental friendliness, cost-effectiveness, and robust electrochemical performance in storing alkaline metal ions.<sup>[23–28]</sup> Both Sn and Sb exhibit high theoretical capacity, excellent electrical conductivity, and low working potential, which have attracted significant interest from researchers since 2012. However, their application is severely limited by sluggish reaction kinetics and substantial volume expansion. Notably, the large volume expansion leads to particle coarsening and loss of contact between the active materials and the conductive matrix, which directly contributes to rapid capacity fading and slower reaction kinetics. Bi exhibits a high theoretical volumetric specific capacity (3773 mAh cm<sup>3</sup>) and high electrical conductivity ( $7.7 \times 10^6$  S m<sup>-1</sup>), which are critical for constructing compact batteries. The large interplanar spacing ( $d_{003} = 3.95$  Å), as shown in Figure 2, facilitates efficient electron/ion transport and benefits for structural stress relaxation. Although Bi does not outperform silicon and graphite in LIBs, it demonstrates exceptional sodium storage performance, with up to 97% utilization of theoretical capacity, a high-rate capability of 200 C, and stable operation for over 3000 cycles in appropriate electrolytes. Unlike lighter pnictogens, Bi has a suitable reaction potential relative to Na/Na<sup>+</sup>, which minimizes the risk of sodium plating on anodes, thereby enhancing the

safety and longevity of SIBs. Furthermore, the ability of Bi-based materials to achieve high capacities without the necessity for conductive matrices, due to their inherent semimetallic nature, further enhances their appeal as anode materials. These properties make Bi an attractive choice in SIB research and propel its investigation in other energy storage solutions as well.

Despite these promising advantages, Bi-based materials face significant challenges that hinder their practical application. The most critical issue is the drastic volume changes (up to 244%) during cycling, which causes severe mechanical stress, unstable reaction interfaces and finally formed fragile SEI films. Moreover, these fragile SEI films are ineffective at particle coarsening which consumes the electrolyte and contributes to the formation of even more fragile SEI layers, ultimately leading to battery failure. Besides, the severe volume expansion results in structural instability and capacity degradation over time. Additionally, while Bi-based compounds like chalcogenides and oxyhalides, which operate via conversion mechanisms, offer ultra-high capacity and can partially mitigate mechanical stress through in-situ generation of sodium storage substrates, they suffer from irreversible conversion reactions, compromising the stability of sodium storage. Despite advancements in interface optimization and internal electric field construction aimed at improving reaction kinetics, the stability of interphases during repeated sodiation and desodiation remains challenging. Furthermore, while the electrochemical properties of Bi-based materials are superior, the complicated synthesis requirements and potential cost implications also present practical challenges towards wide commercialization in energy storage systems.



Lina Zhao received her Ph.D. degree in School of Materials Science and Engineering in University of Science and Technology Beijing in 2019. She worked at College of Engineering, Peking University as a postdoctoral fellow from 2019–2021. Now, she joins in School of Environmental and Chemical Engineering, Shenyang University of Technology. Her main research interests focus on the development of novel nanomaterials for electrochemical energy storage and conversion devices, in particular Na/K ion batteries and spent battery recyclization.



Yuhao Wen is working on bismuth-based anode materials for sodium ion batteries as a master student majoring in chemical engineering and Technology in the School of Environmental and Chemical Engineering at Shenyang University of Technology.



Haitao Zhang earned his Ph.D. degree from the University of Sciences and Technology of China in 2006. After that, he conducted his postdoctoral research in National University of Singapore and National Institute for Materials Science (NIMS, Japan). Since 2012 he has been assigned as a professor in the Institute of Process Engineering, Chinese Academy of Sciences. His current research interests focus on the new energy materials, energy storage techniques, and recyclization of spent battery recyclization. He has authored or co-authored more than 150 papers in peer reviewed SCI journals, such as *Adv. Mater.*, *Phys. Rev. Lett.*, *Energy Storage Mater.*, *Adv. Funct. Mater.*, *Chem. Mater.*, et al.

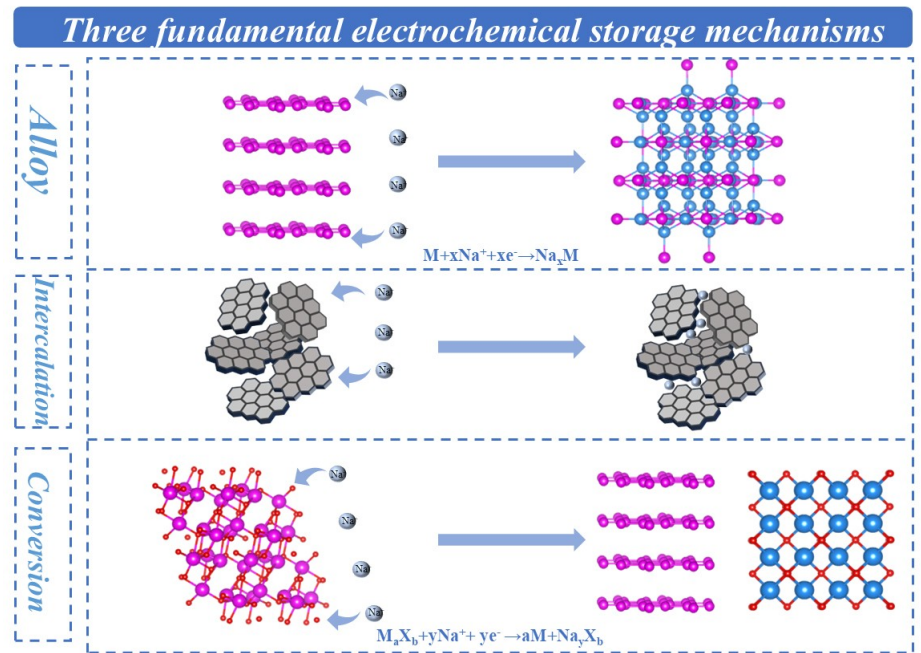


**Figure 1.** The schematic illustration of three fundamental electrochemical storage mechanisms of SIB anode materials.

Element	Bi	RP	Sn	Sb
Final Sodiation Product	$\text{Na}_3\text{Bi}$	$\text{Na}_3\text{P}$	$\text{Na}_{15}\text{Sn}_4$	$\text{Na}_3\text{Sb}$
Theoretical Specific Capacity (mAh g <sup>-1</sup> )	385	2596	847	660
Volume Expansion Rate (%)	244	490	423	393
Electronic Conductivity (S m <sup>-1</sup> )	$7.7 \times 10^6$	$1.0 \times 10^{-14}$	$9.1 \times 10^6$	$2.6 \times 10^6$

**Figure 2.** Comparison of basic electrochemical characteristics of Bi, P, Sn and Sb.

### 3. Structure Regulation Strategies

The complexity of the electrochemical reaction mechanisms influencing sodium storage performance arises from multiple factors, including ionic/electronic conductivity, interphase side reaction and phase transition. Accordingly, structure design for electrode materials is essential in addressing the challenges associated with their unstable interfaces and slow electrons/ions transport kinetics. To achieve high capacity and stable cycling, significant efforts have been devoted to enhancing battery electrochemistry through innovative design of structures and components, including electrode materials, elec-

trolytes, separators, and current collectors. From the perspective of Bi-based anodes development, modification strategies primarily focus on adjusting components, enhancing activity, and mitigating side reactions and phase transitions. The subsequent section will discuss recent advances and analyze the underlying mechanisms of these strategies, categorized into four methods: nanostructure optimizing, surface engineering, morphology modifying and composition regulating (Figure 3).

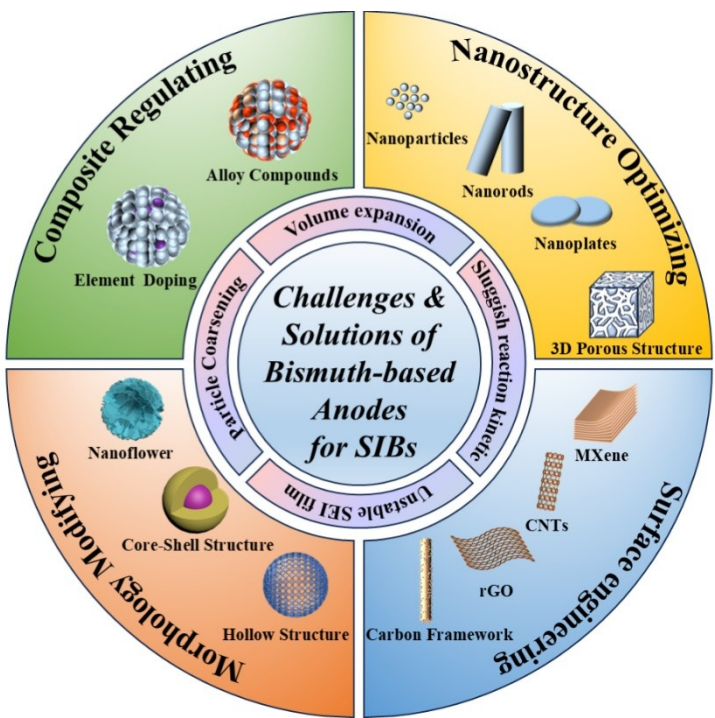


Figure 3. Schematic illustration of challenges and solutions of Bi-based anodes for SIBs.

### 3.1. Nanostructure Optimizing

Benefiting from the extensive advantages of nanotechnology, nanocrystallization presents a promising approach to enhancing the sodium storage capabilities of SIB electrode materials by improving kinetics, thermodynamics, and the  $\text{Na}^+$  storage reactivity. Reducing particle size intuitively shortens the  $\text{Na}^+$  transport path, thereby reducing the average diffusion time and improving diffusion kinetics. Additionally, although the increased contact area between the electrode material and the electrolyte can lead to the excessive formation of SEI films which may decrease the ICE, it facilitates greater involvement of active materials in  $\text{Na}^+$  storage, thereby enhancing specific capacity. Furthermore, the enlarged contact area contributes to higher reactivity and reduced polarization during the sodiation and desodiation processes.

Jae-Chul Lee et al.<sup>[29]</sup> demonstrated that the initially destructive fragmentation structure of bulk Bi particles can be effectively transformed into desirable nanoparticles (NPs) after repeated  $\text{Na}^+$  insertion and extraction in ethylene glycol dimethyl ether (DME)-based electrolyte. Commercial bulk Bi particles with sizes ranging from 1–10  $\mu\text{m}$ , used without any pre-treatment, served as the anode material for SIBs. Remarkably, the initial smooth Bi particles/flakes (Figure 4a,e) evolved into a loosely connected Bi NP nanostructure (Figure 4b,f), which subsequently developed into a 3D porous framework with significant voids and thin struts (Figure 4c,d,g,h). The unique characteristics of the porous Bi nanostructure significantly enhanced the practical capacity (382 and 379  $\text{mAh g}^{-1}$  at 10 C and 20 C, respectively; 1 C = 385  $\text{mA g}^{-1}$ ), stable cycling

(6000 and 3500 cycles 10 C and 20 C, respectively), and rate performance (94% and 93% capacity retention at ultrahigh 80 C and 100 C) of the Bi anodes. DFT calculation results indicate that low electrical resistivity and high Na diffusivities of intermediate phases ( $\text{NaBi}$  and  $\text{Na}_3\text{Bi}$ ) are key factors enabling the unprecedent sodium storage performance (Figure 4i–k).

### 3.2. Surface Engineering

As nanocrystallization significantly increases the specific surface area, it often leads to undesirable side reactions. To address this challenge, considerable efforts have been made to protect the active surface from electrolyte attack. Among these efforts, surface engineering emerges as a widely adopted and effective strategy, particularly for alloying-type anode materials.<sup>[29–31]</sup> The primary mechanisms through which surface engineering enhances electrochemical performance include: (1) Surface coating layer acts as physical barriers that prevent direct contact between electrode materials and the electrolyte solution, thereby protecting against corrosive HF attack. These protective layers also help to suppress the dissolution of active materials and enhances structural stability. (2) Appropriate coating layer facilitates the formation of a thin, stable solid-electrolyte interphase (SEI), leading to improved Coulombic efficiency and extended cycle life. (3) Coatings composed of conductive materials can improve electron/ion transfer on the active material surface, thereby boosting overall electrochemical performance. This section summarizes the surface engineering strategies for nanostructured Bi-based electrode materials, with

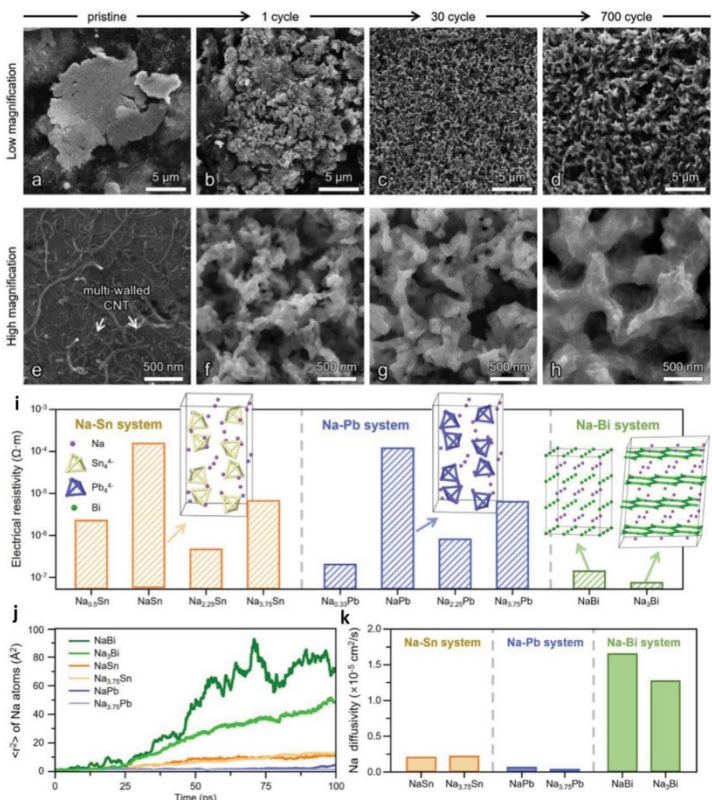


**Figure 4.** a-h) SEM images of the morphological evolution of the 3DPBi anodes during different sodiation/desodiation cycles. DFT calculation results of i) electrochemical resistivity, j)  $\langle r^2 \rangle$  values of Na atoms, and k) Na diffusivities of different sodiation intermediate phases in metallic Sn, Pb and Bi anode. Reproduced with permission from Ref. [29]. Copyright 2022 Wiley-VCH.

particular emphasis on techniques such as *in-situ* carbon coating and conductive matrices compositing.

### 3.2.1. In-Situ Carbon Coating

Carbon coating is widely recognized as an effective approach to enhance electronic conductivity, preserve structural integrity, and promote the formation of stable SEI layers associated with nanostructured materials.<sup>[32]</sup> *In-situ* carbon coating process, the carbonization of carbon-containing precursors occurring simultaneously with the formation of crystalline structures, effectively limits the size of the primary particles of electrode materials, ensuring a uniform and comprehensive coating.

Firstly, bismuth-containing organic salts undergo high-temperature decomposition, leading to the transformation into amorphous carbon that *in-situ* covers the surface of Bi-based nanocrystals. Zhao et al.<sup>[33]</sup> presented a novel particle-in-bulk structure with Bi nanospheres embedded in N-doped carbon (denoted as BiNC) using bismuth ammonium salt complex (Bi(NH<sub>3</sub>)<sub>2</sub>C<sub>6</sub>H<sub>5</sub>O<sub>7</sub>) as the precursor via a straightforward two-step annealing process, as depicted in Figure 5a. Their findings revealed that the unique inlaid architecture (Figure 5b) effectively transfers the stress and strain resulting from volume changes from the Bi nanospheres to the surrounding carbon matrix. Furthermore, DFT simulations of the volume-expansion-

resistance mechanism during the bismuth dealloying process, considering varying degrees of stiffness (which correspond to different out-of-plane stresses), confirm that compressive stress (~10%) generated by the surrounding bulk carbon can induce a “domino-like” recovery of Bi crystals, thereby maintaining the structure’s impressive stability (Figure 5c). As a result, the synthesized BiNC demonstrates a record-high volumetric capacity (823.1 mAh cm<sup>-3</sup>), exceptional initial Coulombic efficiency (95.3%) along with unprecedented rate capability (Figure 5d), outperforming the state-of-the-art literature. In addition, Xu et al.<sup>[34]</sup> reported a nanosized Bi@C composite which was synthesized using a straightforward annealing process with commercial bismuth citrate as the coordination compound precursor (Figure 5e). At an elevated temperature of 900 °C, the organic ligands in the bismuth citrate precursor were converted into amorphous carbon (Figure 5f), while the bismuth core was melted into liquid Bi metal due to its low melting point (271 °C). During the cooling process, the newly formed carbon framework effectively restricted the growth of Bi, leading to the formation of single nanocrystalline Bi (Figure 5g,h). The resulted Bi@C composite exhibited remarkable sodium-storage performance, with an ultralong cycle life of 30,000 cycles at a high current density of 8 A g<sup>-1</sup> and an impressive rate capability, retaining 71% of its capacity at an ultrahigh current rate of 60 A g<sup>-1</sup> (Figure 5i). Even at a high mass loading of 11.5 mg cm<sup>-2</sup>, a stable reversible capacity of 280 mAh g<sup>-1</sup> was

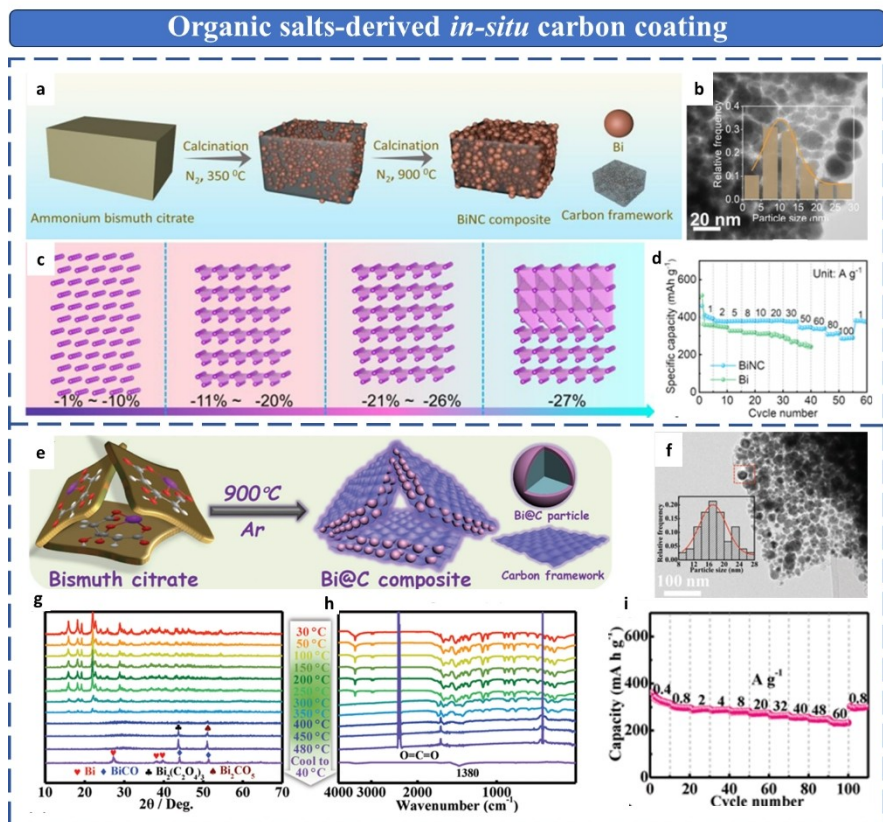


**Figure 5.** Organic salts-derived *in-situ* carbon coating: a) Schematic illustration for the formation of bulk BiNC using  $\text{Bi}(\text{NH}_3)_2\text{C}_6\text{H}_7\text{O}_7$  as the precursor. b) TEM image of the BiNC. c) DFT simulation of the structure evolution with increasing the out-of-plane strain. d) Rate performance of the BiNC anode for SIBs. Reproduced with permission from Ref. [33]. Copyright 2024 Wiley-VCH. e) Schematic illustration of synthesizing Bi@C using bismuth citrate as the precursor. f) TEM image of the Bi@C. g) *In-situ* high-temperature XRD and h) *In-situ* high-temperature FTIR patterns of bismuth citrate calcination. i) Rate performance of the Bi@C for SIBs. Reproduced with permission from Ref. [34]. Copyright 2019 Wiley-VCH.

maintained after 200 cycles. Notably, full SIBs paired with a  $\text{Na}_3\text{V}_2(\text{PO}_4)_3$  cathode also demonstrated exceptional performance.

Secondly, the pyrolysis of polymers is regarded as another crucial method for archiving *in-situ* carbon coating.<sup>[35,36]</sup> Well-dispersed Bi nanoparticles embedded in carbon nanofibers (Bi/C nanofibers) were synthesized through a single-nozzle electrospinning technique followed by carbothermal reduction.<sup>[37]</sup> This inimitable embedded structure afforded an extended cycle life and favorable rate performance for SIBs, which are attributed to the 1D carbon nanofiber architecture and the uniform dispersion of Bi nanoparticles within the carbon matrix. Significantly, the carbon nanofiber (CNF) network structures obtained by electrospinning method can form a strong bond with Bi-based clusters, providing an excellent framework that ensures mechanical protection and facilitates rapid charge transport. In another work, Jiang et al.<sup>[38]</sup> developed a unique ball-cactus-like Bi nanoparticles encapsulated in nitrogen-enriched carbon nanonetworks synthesized via electrospinning (Figure 6a). Through morphology evolution observations shown in Figure 6b–g, the ball-cactus-like Bi nanospheres progressively evolved into a 3D porous nanonetwork during cycling and feature multiple interfaces, which enhances the utilization of active materials, reduces the ion/electron diffusion distance, and boosts pseudo-

capacitive contributions for energy storage. In addition, free-standing bismuth/CNF composites can be fabricated using the electrospinning technique, broadening its potential applications in the field of flexible electronics.<sup>[39,40]</sup>

Furthermore, it is well-established that metal-organic frameworks (MOFs) materials can provide atomic dispersion of metal sites, thus well-distributed metallic nanoparticles coated with carbon materials can be feasibly derived from these frameworks.<sup>[42,43]</sup> Xiong's group<sup>[41]</sup> successfully synthesized a 3D porous hard carbon framework superstructure, composed of 2D ultrathin carbon nanobelt arrays with incorporated metallic Bi nanospheres coated in carbon layers (referred to as Bi@C $\subset$ CFs), via a one-step thermolysis of 1D MOF nanorods (Figure 7a,b). The crosslinked carbon frameworks originating from organic ligands not only exhibited high electronic conductivity, enabling rapid electron transport, but also possessed high porosity and a large surface area, which facilitate convenient electrolyte penetration. Additionally, through a series of spectroscopy observations (Figure 7c) and HUMO and LUMO energy levels calculations as well as *in-situ* structure evolution examinations (Figure 7d–f), the authors further confirmed that ether-based electrolytes were more conducive to forming thinner and more uniform SEI films on the surface of Bi@C $\subset$ CFs compared to ester-based electrolytes. Owing to the robust porous carbon-

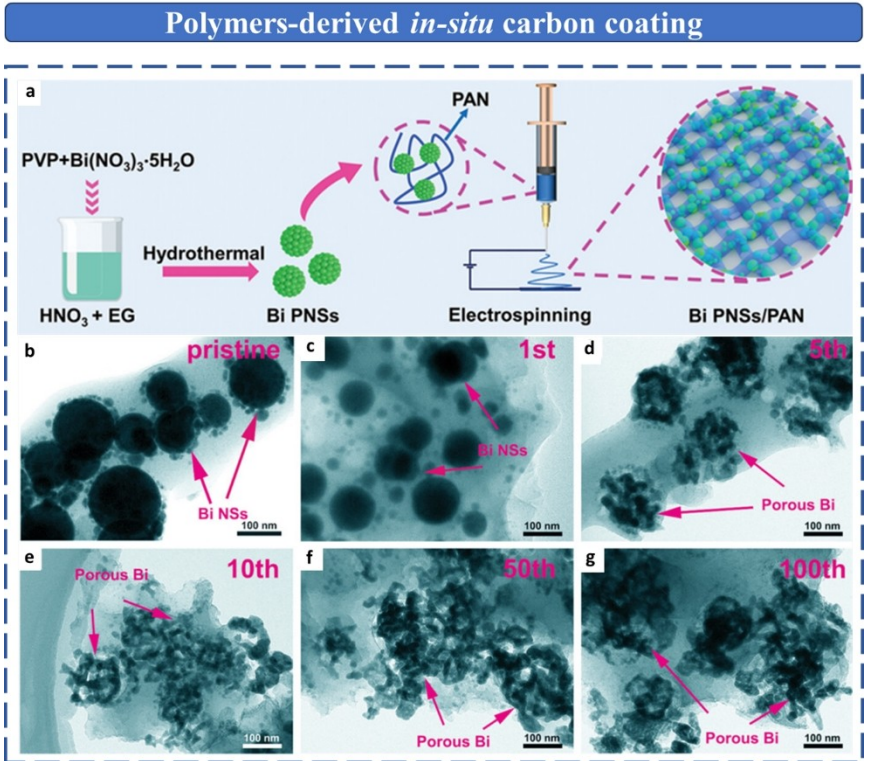


**Figure 6.** Polymers-derived *in-situ* carbon coating: a) Graphic description of the synthesis route of the Bi NSs/NCNs. b–g) TEM images of the Bi NSs/NCNs electrode after different cycles. Reproduced with permission from Ref. [38]. Copyright 2021 Wiley-VCH.

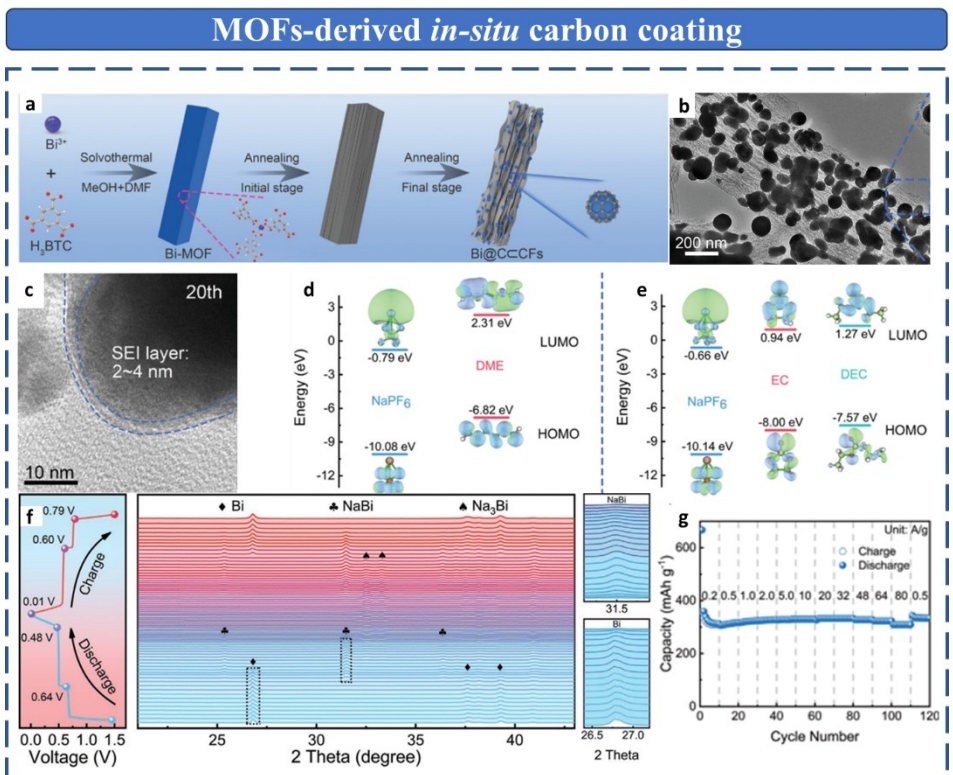


**Figure 7.** MOFs-derived *in-situ* carbon coating: a) Schematic illustration and b) TEM image of the Bi@C@CFs. c) HRTEM of Bi@C@CFs after 20 cycles in DME-based electrolyte. d, e) HOMO and LUMO energy levels of different electrolyte. f) *In-situ* XRD patterns and g) rate capability of Bi@C@CFs. Reproduced with permission from Ref. [41]. Copyright 2021 Wiley-VCH.

coated structure and stable SEI film, Bi@CCCFs anode for SIBs displayed an exceptional long-term cycling stability ( $305 \text{ mAh g}^{-1}$  after 5000 cycles at  $5 \text{ A g}^{-1}$ ) and an impressive rate capability ( $308.8 \text{ mAh g}^{-1}$  even at  $80 \text{ A g}^{-1}$ , Figure 7g). Moreover, when paired with an organic cathode, the full cell (denoted as Bi@CCCFs//PTCDA@450) achieved a high capacity of over  $272 \text{ mAh g}^{-1}$  after 200 cycles at  $1 \text{ A g}^{-1}$ . In another work, Wei et al.<sup>[44]</sup> reported a composite of Bi nanoparticles@N-doped carbon obtained from Bi-MOF precursor using 4,4-bipyridine and 1,3,5-benzenetricarboxylic acid as double ligands, showing considerable sodium storage capability in both Na half-cells and  $\text{Na}_3\text{V}_2(\text{PO}_4)_3$ -coupled Na full-cells.

### 3.2.2. Conductive Matrices Compositing

In order to mitigate volume changes and enhance electrical conductivity simultaneously, the formation of composites that integrate conductive matrices with pristine components has been regarded as one of the most rational structural design strategies. By embedding active components with highly conductive matrices such as carbon nanotubes (CNTs), graphene (rGO), MXenes or conductive polymers, the conductive pathway between the electrodes and current collectors can be

well maintained, significantly inhibiting electrolyte decomposition and promoting the effective charge carrier diffusion.<sup>[45,46]</sup>

A layer-structured  $\text{Bi}_2\text{S}_3$  and CNTs composite exhibited remarkable Na-ion storage capabilities compared to the pure  $\text{Bi}_2\text{S}_3$ .<sup>[47]</sup> The superior performance of this hybrid originated from the  $\text{Bi}_2\text{S}_3$ @CNTs network, which ensured robust structural integrity, high conductivity, and efficient mass transport. Yin et al.<sup>[48]</sup> proposed a green approach for synthesizing Bi-CNTs composite through the electrochemical reduction of  $\text{Bi}_2\text{O}_3/\text{CNTs}$  hybrids in a strong alkaline solution (Figure 8a). The electro-reduction of  $\text{Bi}_2\text{O}_3$  to metallic Bi proceeded by a one-step conversion reaction, during which CNTs could offer abundant reaction sites and build facile electron pathways to accelerate the electro-reduction rate, leading to a smaller grain size of the electrolytic Bi (Figure 8b,c). As a result, the optimized Bi/CNTs composite demonstrated a remarkable Na-storing capacity of  $381.6 \text{ mAh g}^{-1}$  at  $2.0 \text{ A g}^{-1}$  and high initial Coulombic efficiency (81.4%). The architecture of Bi/CNTs network strongly tolerated the mechanical stress associated with the significant volume expansion during the sodiation/desodiation process, thus effectively preventing the abnormal coarsening of Bi particles. The CNTs established robust connections with Bi particles at the Bi/CNTs interface, ensuring fast interfacial charge transfer and structural integrity for charge storage.

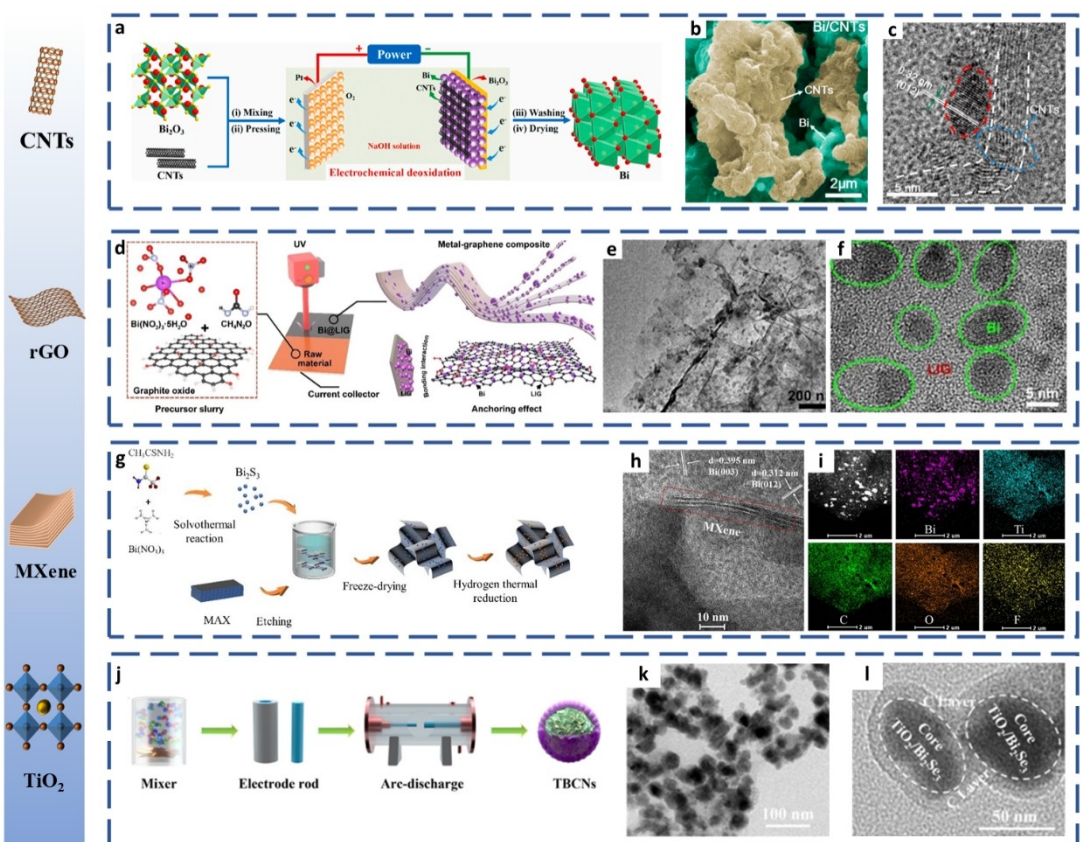


**Figure 8.** Surface engineering with various conductive matrices: a–c) Schematic illustration, SEM and TEM images of the Bi/CNTs composite. Reproduced with permission from Ref. [48]. Copyright 2021 Elsevier. d–f) Schematic illustration, TEM and HRTEM images of the Bi@LiG composite. Reproduced with permission from Ref. [53]. Copyright 2022 Wiley-VCH. g–i) Schematic illustration, HRTEM and HAADF-STEM with EDS mapping images of the Bi/MXene composite. Reproduced with permission from Ref. [54]. Copyright 2021 Wiley-VCH. j–l) Schematic illustration, TEM and HRTEM images of the  $\text{TiO}_2/\text{Bi}_2\text{Se}_3@\text{C}$  composite. Reproduced with permission from Ref. [55]. Copyright 2022 American Chemical Society.

Incorporating Bi-based materials with 2D graphene is widely recognized as an effective approach for enhancing electronic conductivity and preserving structural integrity of the whole electrode, due to graphene's high electronic conductivity and large specific surface area. In order to further promote the electrical contact between the active particles and graphene sheets, double/hybrid carbon coating are often selected.<sup>[49]</sup> Wang's group<sup>[50]</sup> developed a graphene-encapsulated N-doped carbon@Bi (N-C@Bi/G) composites as anode materials for SIBs using a two-step hydrothermal and thermal treatment process, demonstrating an outstanding sodium storage performance. Bi<sub>2</sub>Se<sub>3</sub> nanoflowers anode material, composed of ultra-thin Bi<sub>2</sub>Se<sub>3</sub> nanosheets vertically anchored on rGO via strong C—O—Bi chemical bonds and encapsulated within a N-doped carbon nanolayer (Bi<sub>2</sub>Se<sub>3</sub>@rGO@NC) were also design for highly efficient sodium storage.<sup>[51]</sup> Such hybrid coating strategy is equally effective for potassium-ion batteries (PIBs)<sup>[52]</sup> and aqueous sodium-ion batteries (ASIBs). Yang et al.<sup>[53]</sup> proceeded an indept investigations on the mechanism of enhanced ASIBs cyclability by embedding Bi nanoparticles onto graphene nanosheets via a strong chemical bond, achieved through a novel laser-induced compounding technique (Figure 8d). The Bi nanoparticles were tightly anchored onto the graphene layers through UV laser-induced photochemical reduction, leading to the formation of an inlay structure that can be well served as a buffer matrix to mitigate Bi's volume changes (Figure 8e,f). The strong chemical bond facilitated rapid charge transfer kinetics and greatly improved anode's cyclability, achieving a reversible capacity of 502.6 mAh g<sup>-1</sup> at 250 mA g<sup>-1</sup> and maintaining 122 mAh g<sup>-1</sup> at 4 Ag<sup>-1</sup> over more than 9500 cycles.

Similar to graphene, MXene is a new class of 2D transition metal carbides and/or nitrides, presenting a wide potential for nanostructure synthesizing.<sup>[56,57]</sup> MXenes exhibit a unique combination of properties, such as the high electrical conductivity and mechanical strength, regulable chemical constituent, multi-functionalized surface as well as a high negative zeta potential, making them highly versatile for a wide range of applications. Benefitting from the surface multifunctional groups on MXene, Bi nanoparticles can be tightly anchored on MXene nanosheets through a facile liquid-phase method (Figure 8g-i)<sup>[54]</sup> 2D layered structure of MXene not only provides highly conductive pathways for mass transfer, but also ensures fully contact with electrolyte. Ascribed to the synergistic effect of high conductivity and the pseudo-capacitance of MXene, the designed Bi/MXene composites showed remarkable cycling longevity and fast-charging performance. Furthermore, MXenes are often used as flexible substrates for constructing flexible electrode. For instance, Bi<sub>2</sub>Se<sub>3</sub>/MXene/CNT heterostructures were fabricated via direct physical vapor deposition of Bi<sub>2</sub>Se<sub>3</sub> nanostructures onto a MXene/SWCNT network.<sup>[58]</sup> This composite electrode featured a binder-free characteristic and exhibited commendable sodium-ion storage performance.

Moreover, oxides<sup>[59,60]</sup> and organics<sup>[61]</sup> coatings have been proposed as promising substitutes for carbonaceous layers. It is well known that they undergo limited volume exchange and process considerable mechanical strength, favorable for modifying the surface/interface characteristics to extend the sodium-

storage lifetime. Recently, amorphous TiO<sub>2</sub> outer layers have proven superior to other coatings, primarily due to their inherently isotropic structure and open diffusion channels. As illustrated in Figure 8j, an amorphous TiO<sub>2</sub>/Bi<sub>2</sub>Se<sub>3</sub>@C (TBCNs) nanocomposites were successfully prepared by an arc-discharge method, and a gram-grade yield could be realized.<sup>[55]</sup> Amorphous TiO<sub>2</sub> covered Bi<sub>2</sub>Se<sub>3</sub> were capsuled within the amorphous carbon matrix and were separated by a carbon layer (Figure 8k,l). This configuration led to enhanced Na-ion mobility as well as improved structural stability, which in turn significantly boost both the power density and reactive activity of the inner host materials.

### 3.3. Morphology Modifying

The design of special morphology and crystal orientation of electrode materials plays a critical role in improving the reversible kinetics of alloying/dealloying reactions, reducing diffusion distances, as well as exposing more active surface. To maintain rapid ions/electrons diffusion and structural stability, innovative morphological design strategies are still required. Typically, recent advancements in the structural design of Bi-based anodes can be categorized into 0D, 1D, 2D, and 3D configurations. Different-dimensional structures demonstrate their unique electrochemical capabilities based on surface and structural characteristics.

Typically, 0D Bi-based nanocomposites with yolk-shell, hollow, and core-shell structures have been proposed for high performance SIB anode materials.<sup>[43,70]</sup> Due to the size effect combined with carbon coating, a pomegranate-like Bi@C nanospheres composed of ultrasmall Bi nanoparticles (~7 nm) wrapped uniformly in carbon nanosphere demonstrated excellent sodium storage performance.<sup>[71]</sup> By tailing the core-shell structure, a multicore-shell Bi@N-doped C nanospheres was designed and synthesized (Figure 9a), showing an outstanding electrochemical performance for both SIBs and KIBs. Moreover, through modulating the void size in a yolk-shell structure (Figure 9b), an optimized Bi@Void@C nanospheres SIB anode exhibited an unprecedent rate capability of achieving 173 mAh g<sup>-1</sup> at ultrahigh current of 100 Ag<sup>-1</sup> and impressive cycling stability (~200 mAh g<sup>-1</sup> at 20 Ag<sup>-1</sup> more than 10000 cycles).

1D nanostructure is characterized by a high length-to-diameter aspect ratio, including tubes, rods, wires, and other forms.<sup>[72–76]</sup> Integrating 1D carbon nanostructures with bismuth-based materials can prevent the agglomeration of Bi-based nanoparticles and reduce ion diffusion distances, thereby remarkably improving the electrochemical properties.<sup>[77]</sup> Yang et al.<sup>[64]</sup> reported a hollow Bi nanotube (Bi NT) material via a rational iodine-ion assisted galvanic replacement reaction between Bi<sup>3+</sup> salts with copper nanowires (Figure 9c). Driven by the Kirkendall effect, the designed hollow Bi NTs demonstrated ultrafast and ultrastable sodium storage performance, which can be ascribed to the 1D morphological merit combined with metallic-like nature of Bi. Similarly, as shown in Figure 9d, a microscale hierarchical carbon microtube covered Bi/C compo-

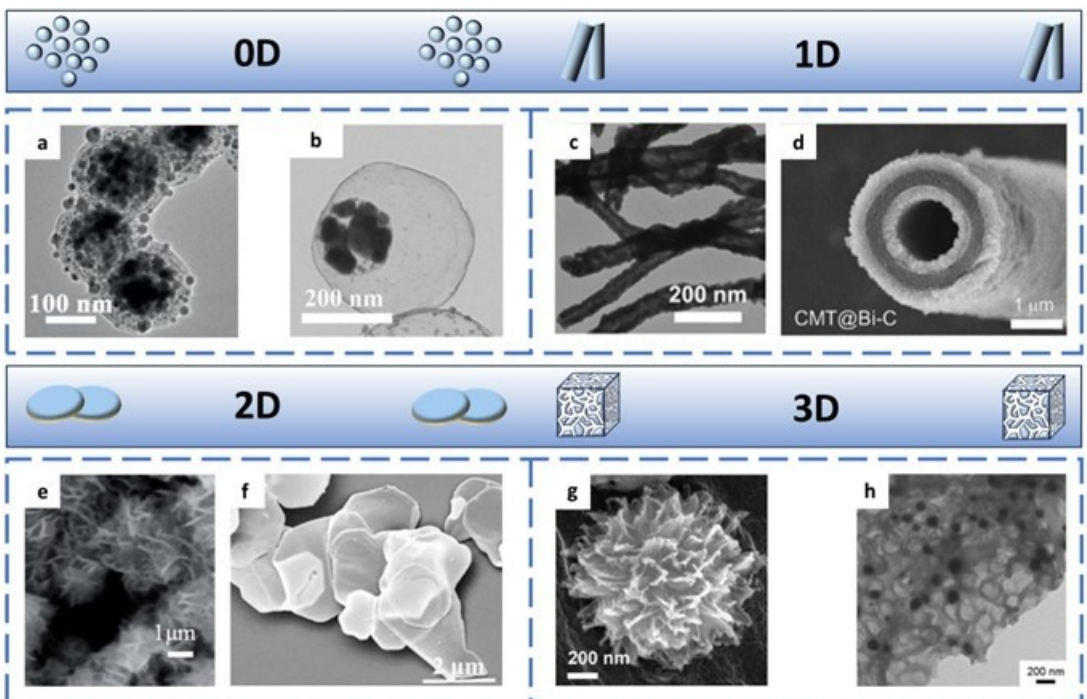


**Figure 9.** Morphology modification for Bi-based electrode materials: a) TEM image of Bi@N-doped C nanocomposite. Reproduced with permission from Ref. [62]. Copyright 2019 Wiley-VCH. b) TEM image of Bi@Void@C material. Reproduced with permission from Ref. [63]. Copyright 2020 American Chemical Society. c) TEM image of Bi NTs. Reproduced with permission from Ref. [64]. Copyright 2022 American Chemical Society. d) Cross-sectional SEM image of CMT@Bi-C composite. Reproduced with permission from Ref. [65]. Copyright 2023 Elsevier. e) SEM image of bismuthene nanosheets. Reproduced with permission from Ref. [66]. Copyright 2020 The Royal Society of Chemistry. f) SEM image of 2D Bi@NOC sheets. Reproduced with permission from Ref. [67]. Copyright 2022 Wiley-VCH. g) TEM image of FBi@NC. Reproduced with permission from Ref. [68]. Copyright 2024 Wiley-VCH. h) TEM image of Bi@3DGFs. Reproduced with permission from Ref. [69]. Copyright 2019 The Royal Society of Chemistry.

site (CMT@Bi-C) was designed for ultrahigh rate SIBs. CMT@Bi-C composites display the structural advantages of a hollow cellular architecture for tolerating the dramatic volume variations during sodiation/desodiation, a core-shell architecture combined with 1D morphology providing a large specific area for fast  $\text{Na}^+$  migration and facile electrolyte penetration.

Compared to 0D and 1D structures, 2D nanomaterials provide a larger surface-to-volume ratio, which greatly enhances electrolyte infiltration.<sup>[77]</sup> Additionally, they offer superior mechanical flexibility, ensuring outstanding structural stability throughout the electrochemical cycling process.<sup>[67]</sup> For instance, Wu's group<sup>[66]</sup> reported a 2D few-layered bismuthene nanosheets (FBNs) through electrochemical exfoliation method (Figure 9e), delivering high capacity and long-term cycling stability for SIBs. Yan et al.<sup>[67]</sup> utilized a hydrothermal approach to synthesize 2D Bi@N-doped C (Bi@NOC) via using BiOBr sheets as the precursor (Figure 9f). The 2D nanostructure exhibits short ion diffusion distance along the radial direction and large contact area between the active material and the electrolyte.

Building 3D interconnected porous architectures can offer abundant ion transport channels, promote the electrolyte infiltration, relieve volumetric strain, inhibit active particles collapsing, as well as generate stable SEI.<sup>[46,78,79]</sup> Therefore, incorporating Bi-based materials into 3D porous networks shows a great promising for constructing high-performance SIB anode materials.<sup>[80]</sup> Yu et al.<sup>[81]</sup> presented a rational strategy of designing a self-healing 3D continuous porous bismuth (3DPBi)

anode for SIBs. The 3DPBi is synthesized via a bottom-up approach, utilizing a liquid phase reduction reaction between bismuth chloride ( $\text{BiCl}_3$ ) and sodium borohydride ( $\text{NaBH}_4$ ). The 3DPBi anode exhibits exceptional sodium storage performance, not only in a Na half-cell showing a superior rate capability ( $352 \text{ mAh g}^{-1}$  at  $60 \text{ A g}^{-1}$ ) and long cyclability (97.6% retention after 3000 cycles at  $10 \text{ A g}^{-1}$ ), but also in a Na-ion full cell coupled with  $\text{Na}_3\text{V}_2(\text{PO}_4)_3$  cathode delivering a cycle life of  $273 \text{ mAh g}^{-1}$  after 150 cycles at  $10 \text{ A g}^{-1}$  and a high gravimetric energy density of  $116 \text{ Wh kg}^{-1}$ . It can be concluded that the outstanding sodium storage capabilities of the 3DPBi anode originate from the synergistic effect of the following factors: (1) the 3D interconnected bismuth nanoligaments provide a shortened ion diffusion pathway and maintain an uninterrupted electronic network. (2) the interconnected voids form a continuous pore network facilitating electrolyte penetration, guaranteeing rapid ion transport. (3) the bicontinuous nanoporous structure enables self-healing resisting the significant volume changes associated with sodiation and desodiation, as demonstrated by both *in situ* and *ex situ* TEM observations, thereby maintaining superior structural integrity.

Zhang and his co-workers synthesized flower-like micro-sized Bi@N-doped C (FBi@NC) composites (Figure 9g), delivering remarkable rate capability ( $\sim 370 \text{ mAh g}^{-1}$  at  $30 \text{ A g}^{-1}$ ) and high tap density ( $2.86 \text{ g cm}^{-3}$ ).<sup>[68]</sup> Through a straightforward, efficient, and scalable *in situ* galvanic replacement method, Yang et al. developed<sup>[82]</sup> a self-supported bismuth microforest (MF) anode,

featuring 3D Bi microtree arrays uniformly grown on porous copper foil. Furthermore, molten salts assisted method<sup>[83]</sup> and solution combustion synthesis approach<sup>[84]</sup> have been proposed for the formation of 3D porous Bi@NC SIB anodes, endowing rapid charge transfer kinetics for facile ions/electrons transportation and robust electrode stability to accommodate the mechanical strain. From the perspective of hybrid matrices, rGO-formed sponges<sup>[69]</sup> and MOFs-derived carbon frameworks<sup>[79]</sup> have been proven to be highly effective for synthesizing 3D porous architectures incorporating Bi-based active particles (Figure 9h). The benefits of these unique structures are significant: (1) The 3D interconnected carbonaceous networks can create defined voids that allow the encapsulated Bi to expand freely without compromising the nanostructure's integrity and continuity. (2) They can offer ionic and electronic conductivity, providing continuous pathways for the transport of both electrons and ions reaching the encapsulated Bi nanoparticles. (3) Embedding of Bi nanoparticles within the 3D frameworks prevents direct exposure to the electrolyte, thereby enhancing Bi's interfacial stability.

### 3.4. Composition Regulating

Composition regulating strategies can optimize the crystal structure of nanostructured electrode materials and minimize

irreversible structural transitions during cycling, thereby improving sodium-ion storage performance. Approaches such as element doping and alloying are recognized as effective methods to enhance the stability of Bi-based SIB anode materials.

#### 3.4.1. Incorporating Non-Metallic Elements

Recently, controlling the composition of electrode material to modulate the interfacial chemistry via triggering the catalytic decomposition of the electrolyte and thus building a powerful SEI turns out to be a creative exploration.

A novel approach of incorporating boron atoms into metallic Bi (referred to as B-Bi) to construct a stable SEI film was employed by Xi and co-workers,<sup>[85]</sup> achieving an ultrastable sodium storage performance. The B-Bi nanoparticles were prepared by through a simple and efficient chemical reduction reaction, as illustrated in Figure 10a. The incorporation of boron catalyzed electrolyte decomposition and promoted the formation of more NaF on the electrode surface, which led to the formation of a stable and mechanically robust SEI layer. DFT calculations further confirmed that the introduction of boron not only enhanced kinetic performance but also facilitated the catalytic decomposition of NaPF<sub>6</sub> and ethylene glycol dimethyl ether at the electrode-electrolyte interface (Figure 10b-d).

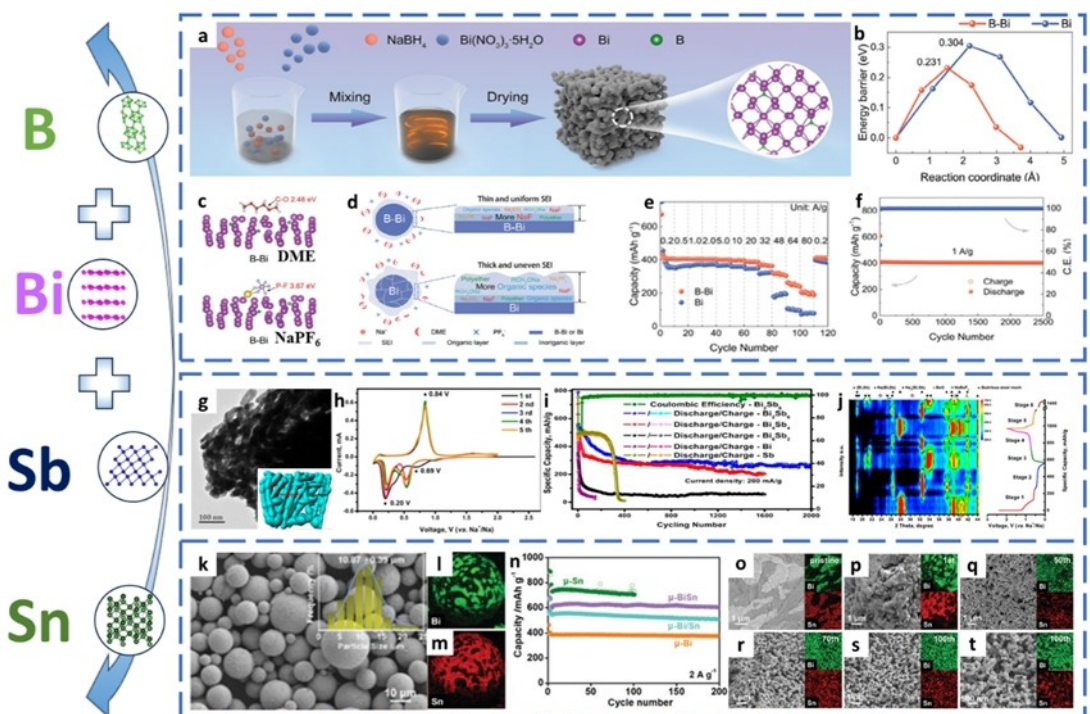


**Figure 10.** a) Schematic illustration of synthesizing B-Bi nanoparticles. DFT calculations of b) migration energy barriers and c) the dissociation energy of electrolyte in B-Bi and Bi. in B-Bi and Bi electrode. d) Schematic illustration of SEI formation in B-Bi and Bi surface. e) Rate capability between B-Bi and Bi. f) Cycling performance of B-Bi. Reproduced with permission from Ref. [85]. Copyright 2023 Wiley-VCH. g) TEM image with schematic description of Bi<sub>2</sub>Sb<sub>6</sub> alloy. h) CV curves of Bi<sub>2</sub>Sb<sub>6</sub> electrode at a scan rate of 0.1 mV s<sup>-1</sup>. i) Cycling performance of Bi<sub>x</sub>Sb<sub>y</sub> with comparison of bare Bi/Sn anodes. j) Operando XRD patterns of Bi<sub>x</sub>Sb<sub>y</sub>. Reproduced with permission from Ref. [86]. Copyright 2018 American Chemical Society. k-m) SEM image of μ-BiSn and corresponding EDS mappings. n) Cycling behavior comparison of μ-BiSn, μ-Bi, μ-Bi/Sn and μ-Sn anodes. o-t) SEM images and element mappings of μ-BiSn before and after cycling with different cycle numbers. Reproduced with permission from Ref. [87]. Copyright 2022 The Royal Society of Chemistry.

Consequently, when used as an anode material for SIBs, Bi–Bi demonstrated remarkable impressive rate capability (Figure 10e, ~200 mAh g<sup>-1</sup> at 80 A g<sup>-1</sup>), long-cycling stability (Figure 10f) and significant potential for application in full cells.

### 3.4.2. Alloying with Metallic Elements

To address the issue of material pulverization resulted from the volumetric expansion of alloy-type anodes (e.g., Bi, Sb, Sn), a promising approach involves forming binary<sup>[88,89]</sup> or ternary alloys.<sup>[90]</sup> In these alloys, additional metals act synergistically as buffer substrates, providing numerous active sites, alleviating volumetric strain, and enhancing diffusion kinetics due to their differing reaction potentials and activities. However, a simple alloying strategy alone is insufficient to meet the performance requirements of alloy-type anode materials. Further optimizations, such as nanostructure design or incorporating a 3D conductive carbon matrix, are necessary to improve the electrochemical performance of Bi-based alloys.<sup>[91–94]</sup>

Among such alloys, the Bi<sub>x</sub>Sb<sub>y</sub> alloy has gained great attention as a promising anode material for electrochemical storage due to several key advantages<sup>[95–97]</sup>: (1) the similar properties of Bi and Sb allow the formation of an infinite solid solution, enabling continuous adjustment of alloy composition; (2) a high theoretical capacity of Sb and an unprecedented rate capability of Bi, ensuring that the resulting Bi<sub>x</sub>Sb<sub>y</sub> alloys deliver desirable electrochemical performance; and (3) alloying may enhance mechanical properties, accommodating the significant strain during cycling. As shown in Figure 10g, nanoporous Bi<sub>x</sub>Sb<sub>y</sub> ( $x:y=2:6; 4:4; 6:2$ ) alloys were designed and synthesized through the dealloying of ternary Mg-based precursors.<sup>[86]</sup> As an anode material for SIBs, Bi<sub>x</sub>Sb<sub>y</sub> alloys demonstrated significantly enhanced cycling performance (only 0.0072% capacity loss per cycle at 1 A g<sup>-1</sup> over 10,000 cycles) compared to their monometallic counterparts (Bi or Sb) (Figure 10h,i). The superior performance can be attributed to the nanoporous structure, the synergistic alloying effect as well as the optimized Bi/Sb atomic ratio, which facilitate electrolyte infiltration, enhance electron and ion transport, and collectively mitigate volumetric changes. Based on *operando* XRD analysis (Figure 10j) combined with DFT calculation results, the (de)sodiation mechanism ((Bi,Sb)↔Na(Bi,Sb)↔Na<sub>3</sub>(Bi,Sb)) upon discharging/charging in Bi<sub>x</sub>Sb<sub>y</sub> alloys was identified.

In addition to Sb, Sn is notable for its high theoretical capacity (847 mAh g<sup>-1</sup>), low discharge voltage (~0.4 V vs. Na<sup>+</sup>/Na), excellent electronic conductivity, and non-toxic nature. Consequently, Sn can be regarded as an optimal buffering material for Bi.<sup>[98]</sup> For example, Li et al.<sup>[99]</sup> designed a Bi/Sn@3D-C structure, where Bi and Sn are embedded in ZIF-derived N-doped 3D porous carbon framework, demonstrating excellent Li-ion and Na-ion storage performance. Yang et al.<sup>[87]</sup> synthesized a micro-sized bimetallic BiSn alloy through a ultrasonication process of molten metal at a low temperature. Elemental mapping of Bi and Sn (Figure 10k–m) reveals distinct regions, indicating the immiscibility between the two metals, with a clear boundary between Sn and Bi. Owing to the

synergistic effects, the bimetallic  $\mu$ -BiSn microspheres effectively integrated the high capacity of Sn with the high-rate of Bi, demonstrating superior Na-storing performance characterized by a high ICE of 90.6%, excellent cyclability (~540 mAh g<sup>-1</sup> after 3000 cycles at 2 A g<sup>-1</sup>), and remarkable rate capability (~390 mAh g<sup>-1</sup> at 10 A g<sup>-1</sup>) (Figure 10n). Notably, after multiple cycles, the distribution of Bi and Sn became more uniform than in the original configuration (Figure 10o–t). This *in situ* reconstruction facilitated the synergistic interaction between Bi and Sn. Rather than deactivating the electrode, this unique coral-like nanostructure allowed the alloy anode to accommodate the significant volume variations during cycling and promoted rapid Na<sup>+</sup> transport.

In summary, the key advantages and challenges associated with various structure regulation strategies for enhancing the electrochemical performance of SIB Bi-based electrodes can be concluded as follows:

#### 3.4.2.1. Nanostructure Optimizing

This approach increases the contact area between the electrode and electrolyte, which shortens the Na<sup>+</sup> diffusion path and enhances sodium storage kinetics and reactivity. However, a larger contact area may lead to increased consumption of electrolyte for SEI formation and result in more side reactions.

#### 3.4.2.2. Surface Engineering

This strategy primarily provides effective protective measures, such as surface coatings that act as physical barriers, facilitating the formation of a stable SEI and enhance electron/ion transfer. However, surface modification strategies face several challenges, including ensuring material compatibility, achieving uniform coating thickness, and maintaining long-term stability under operational conditions. Additionally, the cost and scalability of these techniques, as well as potential environmental impacts, pose significant hurdles for their practical application in energy storage systems.

#### 3.4.2.3. Morphology Modifying

This method exposes more active sites and improves the kinetics of reversible redox reactions during sodiation and desodiation. Notably, core-shell structures can effectively limit volume expansion. However, achieving precise morphology modifications can be challenging and may increase production costs.

#### 3.4.2.4. Composition Regulation

This strategy can enhance performance by incorporating unactive elements while preserving structural integrity during prolonged cycling. Nonetheless, the addition of elements may

lead to rapid capacity loss, greater volume expansion, and, in some cases, higher production costs.

## 4. Sodium Storage Mechanisms

Metallic bismuth along with some intermetallic alloys are regarded as promising anode materials for SIBs. Structurally and visually, bismuth bears a strong resemblance to graphite: it is gray, flaky, and features a wrinkled, layered structure composed of hexagonal six-membered rings, classified under the space group  $R\text{-}3\text{ m}$  (No. 166), bonded by weak van der Waals interactions.<sup>[100]</sup> These two-dimensional layers are stacked with substantial interlayer spacing along the  $c$ -axis ( $d_{003}=3.95\text{ \AA}$ ),<sup>[101]</sup> which is ideally suited for accommodating relatively large  $\text{Na}^+$  during insertion and extraction processes. Metallic bismuth serves as an alloy-based anode material, based on the alloying mechanism (Figure 11), whereas bi-based compounds including oxides and chalcogenides primarily follow the conversion-alloy reaction mechanism.

### 4.1. Bismuth Metal

Layered metallic bismuth provides substantial space for the accommodation of  $\text{Na}^+$ . Similar to graphite and other pnicotogens, layered bismuth can be easily exfoliated into few-layered 2D structures, referred to as bismuthene. Like antimonene, bismuthene possesses a high surface area and large interplanar voids, facilitating the diffusion of  $\text{Na}^+$ . Furthermore, repeated cycles of insertion and extraction can induce self-generated porosity within the bulk structure, enhancing structural stability, capacity retention, and overall performance.<sup>[29]</sup> Apart from the structural evolution, the phase transition of Bi during sodiation and desodiation has raised increasing attention, as the reaction pathway is crucial for

understanding the underlying mechanism of structural transformation.

In 2018, Sun et al.<sup>[102]</sup> proposed a single-step intercalation mechanism for nanosized Bi particles based on *ex-situ* XRD analysis, which was further supported by DFT calculations indicating  $\text{Na}^+$  accommodation along the  $c$ -axis of Bi crystals. Recent years, with the rapid development of *operando* synchrotron XRD and X-ray absorption (XAS) spectroscopy and *in-situ* imaging technologies, an alloying mechanism through the processing sequence  $\text{Bi}\rightarrow\text{NaBi}\rightarrow\text{Na}_3\text{Bi}$  when sodium is inserting into bismuth has been well established. At the first stage of the interaction between Na and Bi primarily involves the formation of  $\text{NaBi}$ . However, there remains some debate regarding the precise mechanism of the subsequent phase transition  $\text{NaBi}\rightarrow\text{Na}_3\text{Bi}$ , as claimed by various research findings. In some research studies, the complete redox reactions of Bi in SIBs have been generally considered as a two-stage intercalation and alloying reaction mechanisms ( $\text{Bi}\leftrightarrow\text{NaBi}\leftrightarrow\text{Na}_3\text{Bi}$ ).<sup>[68,103]</sup> As illustrated schematically in Figure 12a-f, both *in-situ* XRD and *ex-situ* HRTEM reveal that the phase transition is highly reversible.

On the other hand, Sottmann et al.<sup>[105]</sup> noted that the phase transition during sodiation was influenced by the initial size of the Bi grains. Nanocrystalline bismuth formed a metastable cubic phase of  $\text{Na}_3\text{Bi}$  ( $c\text{-Na}_3\text{Bi}$ ) on their crystallite surfaces, whereas the formation of hexagonal  $\text{Na}_3\text{Bi}$  ( $h\text{-Na}_3\text{Bi}$ ) in micro-sized Bi grains. The structural differences, including weaker Na–Bi bonds and varied Na coordination to Bi, between the metastable cubic  $\text{Na}_3\text{Bi}$  phase in nanocrystals and the hexagonal equilibrium polymorph that dominates larger crystallites, provide a reasonable explanation for the improved cycling behavior observed in nanostructured Bi anodes. Furthermore, Zeng et al.<sup>[104]</sup> employed *in-situ* TEM observations to reveal the structural and phase transitions of few-layer bismuth nanosheets during  $\text{Na}^+$  intercalation and alloying (Figure 12g-o). Their study identified a multistep phase transition sequence from Bi to  $\text{NaBi}$ , followed by cubic  $c\text{-Na}_3\text{Bi}$  and then hexagonal  $h\text{-Na}_3\text{Bi}$ . This transition involved  $\text{Na}^+$  migration from the interlayer to the in-plane, triggering the structural shift from ABCABC stacking in  $c\text{-Na}_3\text{Bi}$  to ABABAB stacking in  $h\text{-Na}_3\text{Bi}$  (Figure 12p-u). The metastable  $c\text{-Na}_3\text{Bi}$  phase played a crucial role in buffering the significant structural changes toward the thermodynamically stable  $h\text{-Na}_3\text{Bi}$ , shedding light on the origin of bismuth's volume expansion and its impact on the 2D in-plane structure. The lateral ductility of the few-layer bismuth nanosheet effectively mitigated the in-plane mechanical strain caused by  $\text{Na}^+$  migration, proven its high cyclability in SIBs.

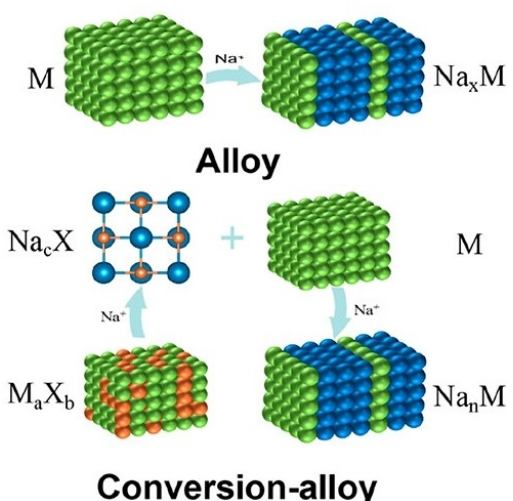
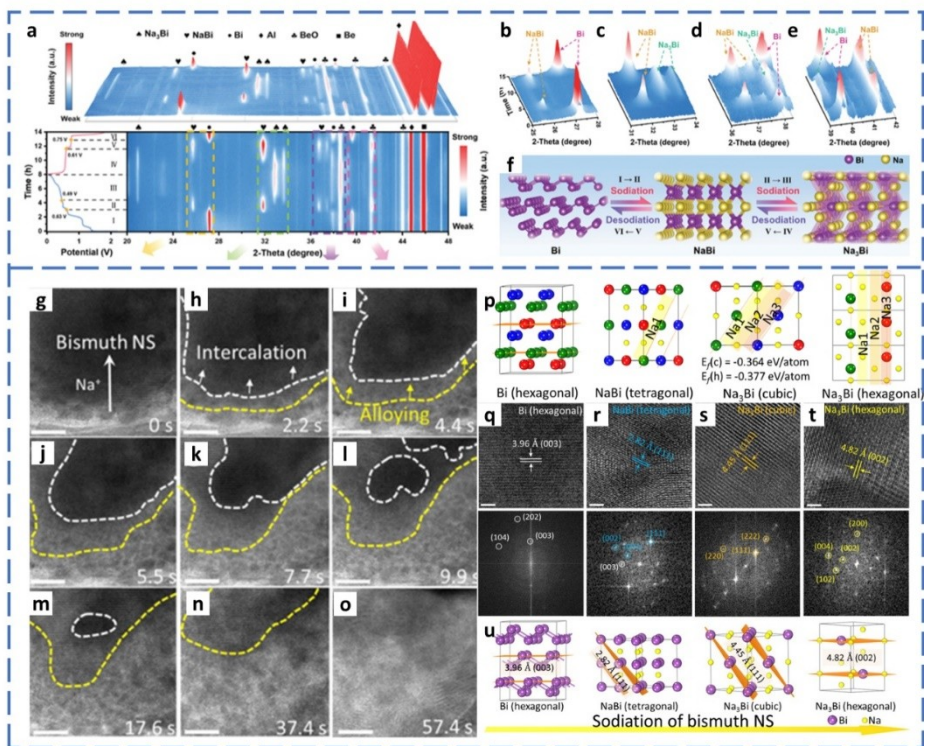


Figure 11. Schematic illustration of alloy and conversion-alloy reaction mechanisms from Ref. [8]. Copyright 2023 American Chemical Society.

### 4.2. Bismuth-Based Chalcogenides

#### 4.2.1. $\text{Bi}_2\text{O}_3$

Bismuth oxide ( $\text{Bi}_2\text{O}_3$ ) has received significant attention due to its high theoretical capacity of  $670\text{ mAh g}^{-1}$ , which is nearly double that of Bi ( $385\text{ mAh g}^{-1}$ ).<sup>[106]</sup> In addition,  $\text{Bi}_2\text{O}_3$  emerges as a promising candidate due to its other notable advantages, such as environmental friendliness, abundant availability, and

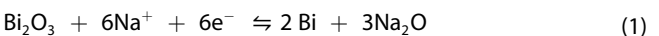


**Figure 12.** Unraveling the sodiation/desodiation reaction mechanism of metallic bismuth: a–e) *In-situ* XRD survey with various diffraction range of FBi@NC anode. f) Schematic illustration of the phase transition processes during  $\text{Na}^+$  insertion/extraction. Reproduced with permission from Ref. [68]. Copyright 2024 Wiley-VCH. g–o) Time-sequences HRTEM images of the Bi NSs anode. p) Atomic structure models of different sodiation interphases. q–t) HRTEM and the corresponding FFT patterns of bismuth NS, NaBi, c-Na<sub>3</sub>Bi, h-Na<sub>3</sub>Bi, respectively. u) Schematic illustration of phase evolution of the Bi NSs anode. Reproduced with permission from Ref. [104]. Copyright 2019 American Chemical Society.

relatively low cost.<sup>[40]</sup> However, most Bi-based materials tend to suffer from electrode fracture and pulverization caused by substantial volume changes, which in turn compromises their cycling stability. However,  $\text{Bi}_2\text{O}_3$  is a significant semiconductor with a band gap of 2.8 eV, limited its electrochemical applications. Furthermore,  $\text{Bi}_2\text{O}_3$  materials tend to suffer from electrode fracture and pulverization caused by substantial volume changes, which in turn compromises their cycling stability.<sup>[107]</sup>

Liu et al.<sup>[108]</sup> proposed a peroxidation-assisted strategy to synthesize  $\text{Bi}_2\text{O}_3$  and electrospun carbon nanofibers ( $\text{Bi}_2\text{O}_3@\text{C-NFs}$ ), utilizing  $\text{Bi}_2\text{S}_3$  nanorods as multifunctional templates (Figure 13a). In their study, bismuth was oxidized by C=O bonds formed during the cyclization reaction in the high-temperature calcination process, effectively preventing carbon from thermal degradation in an oxygen-rich environment at elevated temperatures. Notably, uniformly distributed  $\text{Bi}_2\text{O}_3$  nanodots and longitudinal channels were generated within the S- and N-doped carbon nanofibers (Figure 13b,c). This formation is driven by the continuous diffusion of Bi, produced from the decomposition of  $\text{Bi}_2\text{S}_3$  nanorods, which then converts to Bi–O bonds as the C=O bonds break. Owing to the structural and compositional merits induced by peroxidation strategy, as displayed in Figure 13d–f, the self-supporting  $\text{Bi}_2\text{O}_3@\text{C-NFs}$  anodes exhibited a high specific capacity (~440  $\text{mAh g}^{-1}$  at 50  $\text{mA g}^{-1}$ ), excellent rate performance (~240  $\text{mAh g}^{-1}$  at 20  $\text{A g}^{-1}$ ), and remarkable

cycling stability (~210  $\text{mAh g}^{-1}$  after 2000 cycles at 5  $\text{A g}^{-1}$ ). Compared to the reference samples, the fiber structure and smooth surface morphology of the optimized  $\text{Bi}_2\text{O}_3@\text{C-NFs-600-4 h}$  sample remained well-preserved without any visible cracks (Figure 13g–i), attributed to the effective buffering provided by  $\text{Bi}_2\text{O}_3$  nanodots and longitudinal pores. The phase transformation of  $\text{Bi}_2\text{O}_3$  within  $\text{Bi}_2\text{O}_3@\text{C-NFs-600-4 h}$  during  $\text{Na}^+$  insertion/extraction was analyzed by *in-situ* XRD combined with HRTEM and SAED imaging, as shown in Figure 13j–l. A new peak at 32.3° emerged during discharging, corresponding to the intermediate product  $\text{Na}_2\text{O}$  (JCPDS No. 03–1074). As discharging continued, a peak around 39° appeared, aligning with the (201) crystal plane of  $\text{Na}_3\text{Bi}$  (JCPDS No. 04–0351). Based on the above analysis and related literature, the sodium storage mechanism of  $\text{Bi}_2\text{O}_3$  can be described as follows:



#### 4.2.2. $\text{Bi}_2\text{S}_3$

Bismuth sulfide ( $\text{Bi}_2\text{S}_3$ ) is a V–VI group compound semiconductor known for its narrow band gap of 1.3–1.7 eV and weak

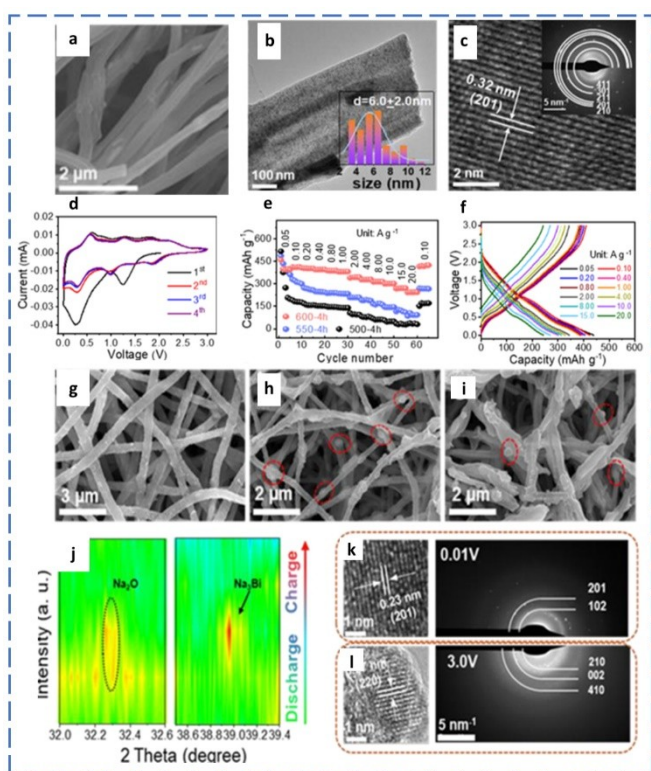
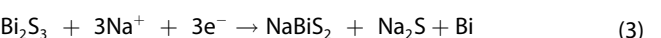


**Figure 13.** a) SEM, b) TEM and c) HRTEM images of  $\text{Bi}_2\text{O}_3@\text{C-NFs}$ -600-4 h. d) CV curves for the first four cycles at a scan rate of  $0.1 \text{ mV s}^{-1}$ . e) Rate performance. f) Discharge/charge curves of  $\text{Bi}_2\text{O}_3@\text{C-NFs}$ -600-4 h at different current densities. g–i) Post mortem SEM images of  $\text{Bi}_2\text{O}_3@\text{C-NFs}$ -600-4 h,  $\text{Bi}@C\text{-NFs}$ -500-4 h,  $\text{Bi}&\text{Bi}_2\text{O}_3@\text{C-NFs}$ -550-4 h after first cycle. j) Contour maps of *ex-situ* synchrotron XRD for the first cycle. k–l) HRTEM and SAED patterns at different voltages. Reproduced with permission from Ref. [108]. Copyright 2023 American Chemical Society.

metal-sulfur bonds,<sup>[109,110]</sup> which enable the long-term storage of  $\text{Na}^+$  through a conversion and subsequent de/alloying process, leading to relatively high specific capacities. Due to its impressive gravimetric and volumetric capacities of  $625 \text{ mAh g}^{-1}$  and  $4250 \text{ mAh cm}^{-3}$ , respectively, for sodium storage,  $\text{Bi}_2\text{S}_3$  has garnered significant interest from researchers.<sup>[111,112]</sup> However, the material experiences substantial volume changes during charging and discharging, causing electrode pulverization and poor cycling stability. Additionally, although sulfides generally exhibit better electron and ion conductivities compared to oxides,  $\text{Bi}_2\text{S}_3$  still fails to meet the conductivity requirements for redox reactions under high current densities, leading to unsatisfactory rate performance in SIBs.

Sun et al.<sup>[114]</sup> first demonstrated the high capacity of  $\text{Bi}_2\text{S}_3$  for sodium storage, revealing that  $\text{Na}^+$  intercalation into  $\text{Bi}_2\text{S}_3$  produces an intermediate  $\text{NaBiS}_2$  phase, which subsequently converts into Bi and  $\text{Na}_2\text{S}$  as observed through *ex-situ* XRD. In contrast, Lu et al.<sup>[115]</sup> clarified that the local microstructure of  $\text{Bi}_2\text{S}_3$  allows for the direct formation of Bi and  $\text{Na}_2\text{S}$  phases without forming the  $\text{NaBiS}_2$  intermediate phase. They also identified that Bi and Na ions undergo further alloying to form a  $\text{Na}_3\text{Bi}$  phase. Recently, Dong et al.<sup>[113]</sup> explored a combination

of *in-situ* TEM, consecutive ED sampling, DFT calculations and FEA modeling to investigate the atomistic origins of  $\text{Na}^+$  interaction behavior and the (de)sodiation mechanisms. The atomic-scale observations revealed a highly anisotropic  $\text{Na}^+$  diffusion pathway, with  $\text{Na}^+$  in  $\text{Bi}_2\text{S}_3$  favoring diffusion along the (110) direction rather than the (200) plane. The electrochemical sodiation process was identified in three distinct stages (Figure 14): i) the initial intercalation reaction forms the  $\text{Na}_x\text{Bi}_2\text{S}_3$  phase, leading to an expansion of the original 2D crystal lattices; ii) the conversion reaction proceeds with the nucleation and growth of  $\text{NaBi}$  and Bi nanoparticles, which remain coherent with the original structure; iii) during deep sodiation, Bi further reacts with Na to form  $\text{Na}_3\text{Bi}$  through an alloying reaction. During desodiation, incomplete reconversion of the  $\text{Na}_2\text{S}$  and Bi phases back to  $\text{Bi}_2\text{S}_3$  was believed to contribute to the initial capacity loss, despite the reversible dealloying of  $\text{Na}_3\text{Bi}$ . Chemo-mechanical simulations using the FEA method further elucidate the deformation and stress evolution induced by the combined effects of mechanical and electrochemical interactions. Based on the analysis presented above and the relevant literature, the sodium storage mechanism of  $\text{Bi}_2\text{S}_3$  can be described as follows:



#### 4.2.3. $\text{Bi}_2\text{Se}_3$

Bismuth selenides ( $\text{Bi}_x\text{Se}_y$ ) exhibit a characteristic layered structure, with Bi and Se atomic layers in a single unit cell arranged alternately along the *c*-axis, while adjacent cells are interconnected via van der Waals forces. This weak interaction, combined with the large interlayer spacing, allows  $\text{Bi}_x\text{Se}_y$  as stable host for  $\text{Na}^+$  accommodation and rapid  $\text{Na}^+$  diffusion.<sup>[116,117]</sup> Compared to their oxide and sulfide analogs, bismuth selenides possess significantly higher conductivity (averaging  $\sim 400 \text{ Scm}^{-1}$ , which is anticipated to enhance sodium storage kinetics.<sup>[118]</sup> Bi and Se can form various stoichiometric structures, such as  $\text{BiSe}$ ,  $\text{Bi}_2\text{Se}_3$ , and  $\text{Bi}_3\text{Se}_4$ . Among these,  $\text{Bi}_2\text{Se}_3$  has received considerable attention due to their high theoretical capacity.

Zhou and co-workers<sup>[119]</sup> precisely regulated the crystalline type and facet orientation of  $\text{Bi}_2\text{Se}_3$  through the ordered guidance of Bi-MOF, effectively controlling metal crystal growth and achieving preferential growth along the (001) facets. The impact of these predominantly exposed facets on sodium storage performance was thoroughly examined. The optimized  $\text{Bi}_2\text{Se}_3-\text{C/G-1}$  sample exhibited a high reversible capacity of  $377 \text{ mAh g}^{-1}$  and excellent rate capability. In addition, a novel strained bismuth selenide material (s- $\text{Bi}_2\text{Se}_3$ ) was synthesized through a post-heat treatment process.<sup>[120]</sup> Its unique structural characteristics, such as expanded interlayer spacing and a narrow band gap, significantly accelerate ion diffusion and electron transfer. The sodium storage mechanism of the s- $\text{Bi}_2\text{Se}_3$

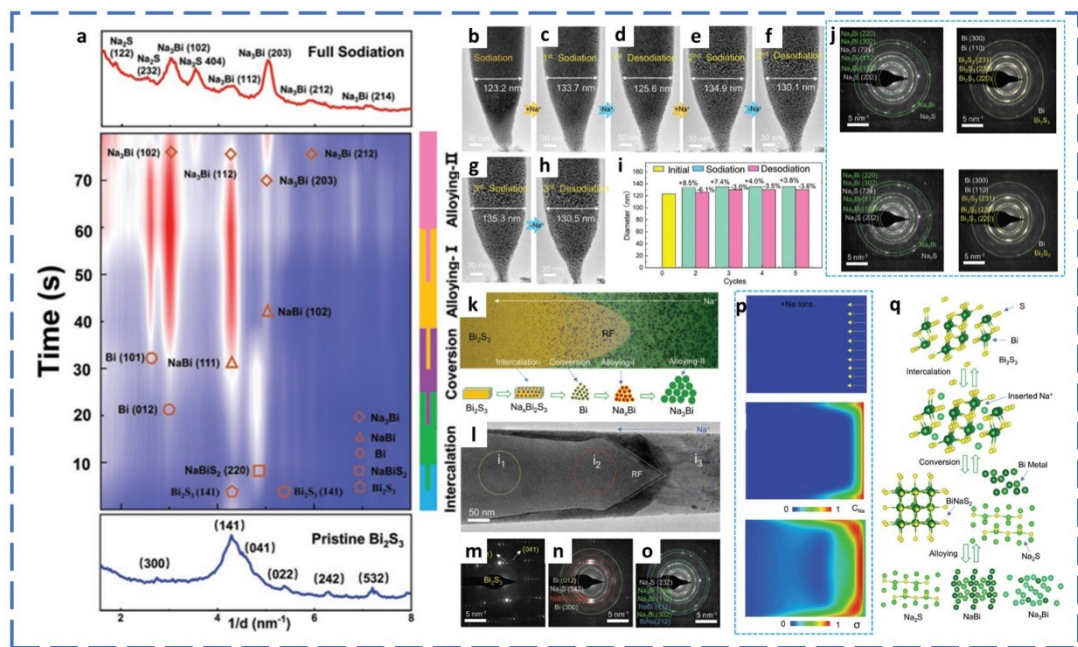


**Figure 14.** a) Contour plots of *in-situ* SAED patterns of  $\text{Bi}_2\text{S}_3$  nanorod. b–h) *In-situ* TEM images of  $\text{Bi}_2\text{S}_3$  during the first three sodiation/desodiation cycles. i) The measured diameters as cycling times of  $\text{Bi}_2\text{S}_3$  nanorod. j) SAED patterns of sodiation–desodiation products at the first and the second cycles. k) Schematic illustration of nanoparticles growth along with phase transformation process during sodiation. l) TEM image indicating nanoparticles growth. m–o) The corresponding SAED patterns in (i). p) FEA modeling results. q) Schematic illustration of the multi-stage sodiation–desodiation mechanism of  $\text{Bi}_2\text{S}_3$ . Reproduced with permission from Ref. [113]. Copyright 2022 Wiley-VCH.

electrode was investigated using ex-situ XRD analysis. Initially, the s- $\text{Bi}_2\text{Se}_3$  undergoes a multi-step conversion reaction ( $\text{s-Bi}_2\text{Se}_3 + \text{Na}^+ \leftrightarrow \text{NaBiSe}_2 + \text{Bi} \leftrightarrow \text{Na}_2\text{Se} + \text{Bi}$ ), followed by a sequential alloying/dealloying process ( $\text{Bi} + \text{Na}^+ \leftrightarrow \text{NaBi} \leftrightarrow \text{Na}_3\text{Bi}$ ). Notably, the  $\text{NaBiSe}_2$  peaks are barely visible, likely due to their low crystallinity. Additionally, the active material cannot be completely restored to s- $\text{Bi}_2\text{Se}_3$  after a full cycle, indicating that the conversion reaction between s- $\text{Bi}_2\text{Se}_3$  and  $\text{Na}^+$  to form  $\text{NaBiSe}_2$  and Bi is irreversible.

#### 4.4. Heterostructures of Bismuth-Based Materials

Constructing heterostructures can significantly enhance reaction kinetics by combining the advantages and mitigating the limitations of different components.<sup>[121,122]</sup> Primarily, heterostructures increase thermodynamic stability by inducing lattice distortions and long-range disorder within the material. Moreover, the redistribution of electrons at phase boundaries can create additional active sites, leading to an enhanced adsorption capacity of  $\text{Na}^+$  and accelerated charge transfer behavior. Additionally, structural stability can be improved through strong interfacial interactions, leading to an extended lifespan. However, constructing nanoscale heterostructures remains challenging due to the difficulty in achieving ideal heterointerfacial contact across all nanocrystals. Nevertheless, recent Bi-based heterostructures demonstrate superior electrochemical storage capabilities due to various synergistic effects.<sup>[112,123–125]</sup>

A distinct heterostructure comprising Bi nanoparticles embedded within  $\text{Bi}_2\text{S}_3$  nanorods was synthesized using a straightforward approach (Figure 15a). This Bi- $\text{Bi}_2\text{S}_3$  heterostructure effectively generated a robust built-in electric field by modulating the energy band structure (Figure 15b,c). The synergistic effect of the established built-in electric field and the strong coupling between Bi and  $\text{Bi}_2\text{S}_3$  significantly enhanced charge transfer efficiency, reduced ion-diffusion resistance, and minimized volume changes during the sodiation/desodiation process. Consequently, the Bi- $\text{Bi}_2\text{S}_3$  heterostructure exhibited remarkable cycling stability (retaining 85% capacity retention after 500 cycles at  $1 \text{ A g}^{-1}$ ), as well as maintaining a high reversible capacity of  $456 \text{ mAh g}^{-1}$  even at  $15 \text{ A g}^{-1}$ . An improved sodium storage performance has been also demonstrated in a heterostructure  $\text{Bi}_2\text{O}_3$ - $\text{Bi}_2\text{S}_3$  nanosheets anode.<sup>[126]</sup> As illustrated in Figure 15f,  $\text{Bi}_2\text{O}_3$  is characterized as an n-type semiconductor with a relatively wide band gap of approximately 2.8 eV, whereas  $\text{Bi}_2\text{S}_3$  a typical p-type semiconductor possessing a narrower band gap of about 1.3 eV. In the  $\text{Bi}_2\text{O}_3$ - $\text{Bi}_2\text{S}_3$  heterostructure, p-n heterojunctions could be formed at the interface, creating a built-in electric field directed from  $\text{Bi}_2\text{O}_3$  to  $\text{Bi}_2\text{S}_3$ . During discharging, this electric field was expected to facilitate the migration of  $\text{Na}^+$ . Upon full sodiation,  $\text{Bi}_2\text{O}_3$  converted into  $\text{Na}_x\text{Bi}$  and  $\text{Na}_2\text{O}$ , while  $\text{Bi}_2\text{S}_3$  transformed into  $\text{Na}_x\text{Bi}$  and  $\text{Na}_2\text{S}$ . The sulfide regions ( $\text{Bi}_2\text{S}_3$ -dominated) could release more  $\text{Na}^+$  due to their higher reversibility compared to oxide regions ( $\text{Bi}_2\text{O}_3$ -dominated). Therefore, during the charging process, an electric field is formed from  $\text{Bi}_2\text{S}_3$  to  $\text{Bi}_2\text{O}_3$ , driven by the potential difference,  $\text{Na}^+$  diffusion could be greatly

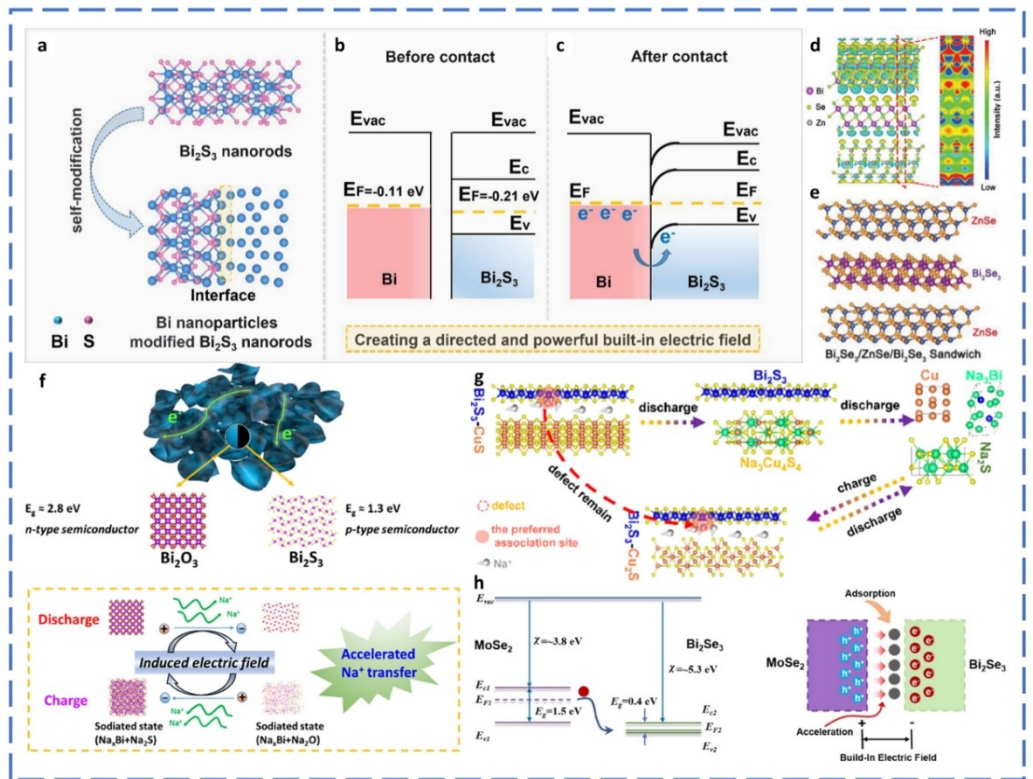


**Figure 15.** Constructing rational heterostructures of Bi-based materials for SIBs: a–c) Schematic illustration of the structural modification and energy band structure of  $\text{Bi}-\text{Bi}_2\text{S}_3$  heterostructure. Reproduced with permission from Ref. [129]. Copyright 2023 Elsevier. d–e) The charge density difference and corresponding heterostructure model of  $\text{Bi}_2\text{Se}_3-\text{ZnSe}$ . Reproduced with permission from Ref. [128]. Copyright 2023 Wiley-VCH. f) Schematic illustration of the built-in electric field mechanism in  $\text{Bi}_2\text{O}_3-\text{Bi}_2\text{S}_3$  heterostructure. Reproduced with permission from Ref. [130]. Copyright 2018 American Chemical Society. g) The structural transformation process of the  $\text{Bi}_2\text{S}_3-\text{CuS}$  heterostructure during cycling. Reproduced with permission from Ref. [127]. Copyright 2023 American Chemical Society. h) Schematic illustration of the built-in electric field and charge redistribution in  $\text{MoSe}_2/\text{Bi}_2\text{Se}_3$  heterostructure. Reproduced with permission from Ref. [131]. Copyright 2021 Wiley-VCH.

enhanced. The induced electric field could also provide a driving force, enhancing charge transfer kinetics and thereby improving rate capability. Moreover, the robust chemical interactions between  $\text{Bi}_2\text{S}_3$  and  $\text{Bi}_2\text{O}_3$  supports the structural elasticity during sodiation/desodiation. Similarly, a heterostructured metal sulfide ( $\text{Bi}_2\text{S}_3-\text{CuS}$ ) supported on carbon was synthesized through calcination and ion exchange techniques.<sup>[127]</sup> Kinetic analysis combined with DFT calculations revealed that the heterointerface (Figure 15g), particularly the sulfur-deficient regions within the  $\text{Bi}_2\text{S}_3-\text{CuS}$  interface, significantly enhanced ion adsorption and facilitated ion transport, attributed to the ultrafast sodiation kinetics.

$\text{Bi}_2\text{Se}_3$ , a three-dimensional topological insulator, exhibits high band velocity and mobility, attributed to its topologically protected surface states. A novel  $\text{Bi}_2\text{Se}_3-\text{ZnSe}$  heterostructure was reported as an outstanding fast-charging material for  $\text{Na}^+$  storage.<sup>[128]</sup> Ultrathin  $\text{Bi}_2\text{Se}_3$  nanoplates with abundant topological insulator metallic surfaces were incorporated as an electronic framework within the material, significantly reducing charge transfer resistance and enhancing overall electrical conductivity (Figure 15d,e). Additionally, the numerous crystalline interfaces between two selenides facilitated  $\text{Na}^+$  migration and offered extra active sites. Consequently, the  $\text{Bi}_2\text{Se}_3-\text{ZnSe}$  heterostructure exhibited an exceptional high-rate performance

of  $360.5 \text{ mAh g}^{-1}$  at  $20 \text{ A g}^{-1}$  and maintained high electrochemical stability, delivering  $\sim 318 \text{ mAh g}^{-1}$  after 3000 cycles, outperforming all reported selenide-based anodes. Based on the in-situ XRD analysis and ex-situ HRTEM and SEAD observing,  $\text{Bi}_2\text{Se}_3$  and  $\text{ZnSe}$  can be found at the end of fully charged stage, indicating a complete reversible electrochemical intercalation/alloying reaction mechanism. Similarly, a topological insulator-assisted  $\text{MoSe}_2/\text{Bi}_2\text{Se}_3$  heterostructure was reported, demonstrating an excellent fast charging performance for SIBs.<sup>[128]</sup> The outstanding rate capability can be attributed to several key advantages: (1) The strong chemical bonds at the heterointerfaces induce orbital hybridization, allowing electron delocalization and thereby enhancing electronic conductivity. (2) The differing bandgaps of  $\text{MoSe}_2$  (1.57 eV) and  $\text{Bi}_2\text{Se}_3$  (0.4 eV) generate a built-in electric field near the heterointerfaces (Figure 15h), which provides an additional electric force to accelerate  $\text{Na}^+$  migration. (3) The electron redistribution-induced electrostatic forces improve structural integrity, contributing to enhanced cycling stability even with a small amount of  $\text{Bi}_2\text{Se}_3$  nanosheets. (4)  $\text{Bi}_2\text{Se}_3$  substrate offers superior electron transfer capability and facilitates alloying reactions, thereby achieving high  $\text{Na}^+$  storage capacity during cycling. (5) The broad interlayer spacing of  $\text{MoSe}_2$  accommodates rapid  $\text{Na}^+$  insertion/extraction processes.

## 5. Summary and Perspectives

Bismuth-based materials for SIBs are characterized by their high theoretical capacity, stable alloying reactions with sodium, and relatively low operating voltage, making them attractive anode choices for SIBs. However, they also undergo significant volume expansion during sodiation, which can lead to potential structural degradation and capacity fading. The fragile SEI interface associated with the dramatic volume variation and mechanical strain conflicts the cycling longevity. Moreover, Bi-based chalcogenides possess relatively low electronic conductivity, which can severely limit the rate performance. Furthermore, the synthesis of these materials is often complex and costly, posing challenges for their application in large-scale production.

Based on the unique properties of bismuth-based materials, this review has comprehensively analyzed the recent advancements in the development and optimization of bismuth-based anode materials for SIBs. This work has highlighted the critical role of structural regulation strategies—namely nanostructure optimization, surface engineering, morphology modification, and composition regulation—in enhancing the electrochemical performance of bismuth-based anodes. Figure 16 provides an overview of structural regulation strategies for Bi-based SIB anodes. Each of these strategies offers unique advantages, such as improved diffusion kinetics, enhanced stability of the SEI, increased mechanical flexibility, and stabilized phase transitions during cycling. While significant progress has been made, the sodium storage capabilities of various Bi-based materials are summarized in Table 1. Additionally, this review has emphasized the importance of understanding the underlying energy storage mechanisms, particularly the conversion and alloying reactions during the sodiation/desodiation of bismuth. This mechanistic insight is crucial for informing the design of structural

modifications and for optimizing the overall performance of the anode materials. The synergy between structural engineering and storage mechanism analysis provides a robust framework for developing high-performance anode materials with improved capacity retention, rate capability, and cycling stability.

Based on the unique properties of bismuth-based materials, the modification strategies discussed, and the electrochemical storage mechanisms highlighted in this review, the following perspectives can be proposed for the future development of bismuth-based anode materials for SIBs:

1. *Design of Multi-Functional Nanostructures:* Future research should focus on the design of multi-functional nanostructures that not only enhance sodium-ion diffusion and reaction kinetics but also improve mechanical stability and accommodate volumetric changes. Hybrid structures combining different nanostructural strategies could be particularly effective in achieving these goals.
2. *Advanced Surface Engineering Techniques:* The development of novel surface engineering techniques that allow for precise control over the composition and thickness of protective coatings is critical. These coatings should minimize side reactions, stabilize the SEI, and enhance the overall cycling stability without significantly increasing resistance or complexity in large-scale applications.
3. *Exploration of Doping and Alloying with Novel Elements:* Continued exploration of doping and alloying with novel elements, particularly those that can enhance electronic conductivity and stabilize the bismuth structure during cycling, is essential. Such strategies should aim to optimize the balance between improved electrochemical performance and material cost.
4. *Mechanistic Studies on Sodiation/Desodiation Processes:* In-depth mechanistic studies on the sodiation/desodiation processes in bismuth-based anodes are needed to fully understand the phase transitions and electrochemical behavior during cycling. These insights will guide the design of new materials with better capacity retention and long-term stability.
5. *Scalability and Cost-Effectiveness of Synthesis Methods:* The development of scalable and cost-effective synthesis methods for bismuth-based anode materials should be a priority. This includes exploring green chemistry approaches, reducing energy consumption during synthesis, and finding ways to recycle or reuse materials in the production process. Achieving cost-effectiveness without compromising performance will be key to the widespread adoption of these materials in commercial SIBs.
6. *Selection rules for cathode and electrolyte in full cells:* As previously discussed, Bi-based anodes demonstrate remarkable stability under high current density and exhibit an extended cycle life, rendering them well-suited for fast charging and industrial applications. Additionally, the synergistic interaction between ether-based electrolytes and bismuth facilitates the formation of uniform and thin SEI films, which significantly reduce volume expansion and enhance cycle longevity. Consequently, ether-based electrolytes are favored over alternative types in Bi-based SIB

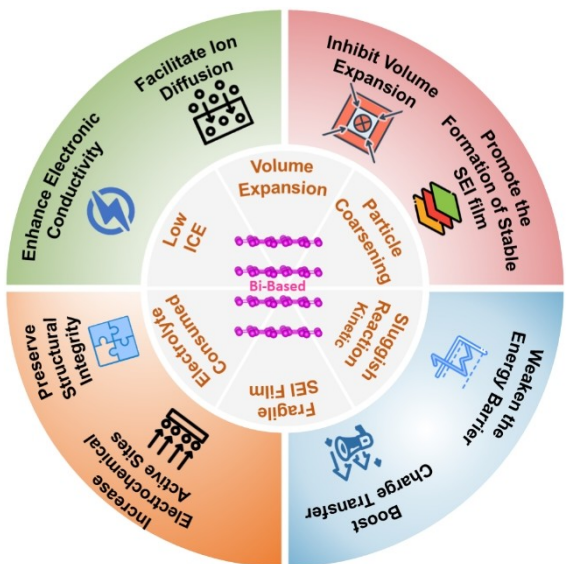


Figure 16. Overview of structural regulation strategies for Bi-based SIB anodes.

**Table 1.** Summary of the sodium storage performance of various advanced Bi-based anode materials for SBs.

Material	Synthesis method	Electrolyte	Cycle performance	Rate performance	ICE	Ref
Bi NPs	Ball mill	1 M NaPF <sub>6</sub> in DME	378 mAhg <sup>-1</sup> after 6000 cycles at 10 Ag <sup>-1</sup>	About 250 mAhg <sup>-1</sup> at 200 C	94%	[29]
Bi/3DPG	Hydrothermal	1 M NaPF <sub>6</sub> in DIGLY/ME	270 mAhg <sup>-1</sup> after 500 cycles at 2 Ag <sup>-1</sup>	266.1 mAhg <sup>-1</sup> at 5 Ag <sup>-1</sup>	60.5%	[52]
LC-Bi	Solvothermal	1 M NaPF <sub>6</sub> in DME	260 mAhg <sup>-1</sup> after 10000 cycles at 1 Ag <sup>-1</sup>	333.4 mAhg <sup>-1</sup> at 100 Ag <sup>-1</sup>	53.4%	[45]
Bi@LNPC	Solvothermal	1 M NaPF <sub>6</sub> in DME	325.4 mAhg <sup>-1</sup> after 4000 cycles at 1 Ag <sup>-1</sup>	285.7 mAhg <sup>-1</sup> at 200 Ag <sup>-1</sup>	52.4%	[46]
BiNC	Thermal treatment	1 M NaPF <sub>6</sub> in DIGLY/ME	320.4 mAhg <sup>-1</sup> after 15000 cycles at 10 Ag <sup>-1</sup>	290.5 mAhg <sup>-1</sup> at 100 Ag <sup>-1</sup>	95.3%	[33]
FBi@NC	Solvothermal	1 M NaPF <sub>6</sub> in DIGLY/ME	378.3 mAhg <sup>-1</sup> after 600 cycles at 1 Ag <sup>-1</sup>	368.2 mAhg <sup>-1</sup> at 30 Ag <sup>-1</sup>	73.6%	[68]
Bi MF	Replacement	1 M NaPF <sub>6</sub> in DIGLY/ME	338.6 mAhg <sup>-1</sup> after 1200 cycles at 1 Ag <sup>-1</sup>	338.9 mAhg <sup>-1</sup> at 50 Ag <sup>-1</sup>	76.5%	[82]
Bi@C-NSA	Galvanic replacement	1 M NaPF <sub>6</sub> in DME	343.7 mAhg <sup>-1</sup> after 200 cycles at 0.05 Ag <sup>-1</sup>	289 mAhg <sup>-1</sup> at 2 Ag <sup>-1</sup>	84.85%	[132]
Bi@NS-C	Solvothermal	1 M NaPF <sub>6</sub> in DIGLY/ME	About 350 mAhg <sup>-1</sup> after 2600 cycles at 1 Ag <sup>-1</sup>	399.5 mAhg <sup>-1</sup> at 30 Ag <sup>-1</sup>	80%	[77]
Bi/CNT	Electrochemical deoxygenation	1 M NaPF <sub>6</sub> in DIGLY/ME	About 280 mAhg <sup>-1</sup> after 5000 cycles at 10 Ag <sup>-1</sup>	399 mAhg <sup>-1</sup> at 5 Ag <sup>-1</sup>	81.4%	[48]
Bi@C	Arc discharge	1 M NaPF <sub>6</sub> in DME	291 mAhg <sup>-1</sup> after 630 cycles at 10 Ag <sup>-1</sup>	318 mAhg <sup>-1</sup> at 10 Ag <sup>-1</sup>	About 80%	[32]
Bi	Bi powder	1 M NaPF <sub>6</sub> in DIGLY/ME	270 mAhg <sup>-1</sup> after 100 cycles at 4 Ag <sup>-1</sup> at 60 °C	173 mAhg <sup>-1</sup> at 200 mAhg <sup>-1</sup> at -40 °C	About 90%	[31]
Bi	Bi powder	1 M NaPF <sub>6</sub> in DIGLY/ME	77 mAhg <sup>-1</sup> after 1600 cycles at 0.2 Ag <sup>-1</sup>	48 mAhg <sup>-1</sup> at 10 Ag <sup>-1</sup>	64%	[30]
Bi@NC	Solvothermal	1 M NaPF <sub>6</sub> in DME	386.2 mAhg <sup>-1</sup> after 400 cycles at 0.2 Ag <sup>-1</sup>	344.1 mAhg <sup>-1</sup> at 5 Ag <sup>-1</sup>	64.5%	[44]
Bi@NC	Solution method	N/A	About 375 mAhg <sup>-1</sup> after 2500 cycles at 5 Ag <sup>-1</sup>	336.7 mAhg <sup>-1</sup> at 20 Ag <sup>-1</sup>	N/A	[80]
Bi@NC-MF	Solution method	1 M NaPF <sub>6</sub> in DME	376 mAhg <sup>-1</sup> after 300 cycles at 1 Ag <sup>-1</sup>	322 mAhg <sup>-1</sup> at 40 Ag <sup>-1</sup>	N/A	[80]
NC@Bi/G	Solvothermal	1 M NaPF <sub>6</sub> in DME	257.6 mAhg <sup>-1</sup> after 1000 cycles at 2 Ag <sup>-1</sup>	246 mAhg <sup>-1</sup> at 5 Ag <sup>-1</sup>	78.87%	[50]
Bi@rGO@NC	Solvothermal	1 M NaClO <sub>4</sub> in EC and DEC (volume ratio 1 : 1) with 5% FEC	90.5 mAhg <sup>-1</sup> after 400 cycles at 0.05 Ag <sup>-1</sup>	84.5 mAhg <sup>-1</sup> at 1 Ag <sup>-1</sup>	About 60%	[52]
Bi NS	Solvothermal	1 M NaPF <sub>6</sub> in DIGLY/ME	330 mAhg <sup>-1</sup> after 1000 cycles at 10 Ag <sup>-1</sup>	348.6 mAhg <sup>-1</sup> at 30 Ag <sup>-1</sup>	About 75%	[38]
CNF-Bi <sub>2</sub> O <sub>3</sub>	Electrospinning	1 M NaClO <sub>4</sub> in PC with 5% FEC	372 mAhg <sup>-1</sup> after 100 cycles at 0.025 Ag <sup>-1</sup>	393 mAhg <sup>-1</sup> at 0.625 Ag <sup>-1</sup>	36.45%	[107]
CMT@Bi-C	Thermal treatment	1 M NaPF <sub>6</sub> in DME	383.3 mAhg <sup>-1</sup> after 1000 cycles at 1 Ag <sup>-1</sup>	189 mAhg <sup>-1</sup> at 200 Ag <sup>-1</sup>	About 97%	[65]
BiPS <sub>4</sub>	Thermal treatment	N/A	410 mAhg <sup>-1</sup> after 1000 cycles at 1 Ag <sup>-1</sup>	322 mAhg <sup>-1</sup> at 5 Ag <sup>-1</sup>	97.7%	[36]
Bi <sub>2</sub> S <sub>3</sub> @Co <sub>9</sub> S <sub>8</sub> /NC	Thermal treatment	N/A	458 mAhg <sup>-1</sup> after 1000 cycles at 1 Ag <sup>-1</sup>	341 mAhg <sup>-1</sup> at 8 Ag <sup>-1</sup>	78.5%	[123]
Bi <sub>2</sub> S <sub>3</sub> @C@Co <sub>9</sub> S <sub>8</sub>	Solvothermal	1 M NaCF <sub>3</sub> SO <sub>3</sub> in DEGDME	417.7 mAhg <sup>-1</sup> after 1600 cycles at 2 Ag <sup>-1</sup>	470.6 mAhg <sup>-1</sup> at 4 Ag <sup>-1</sup>	87.8%	[42]
Bi <sub>2</sub> S <sub>3</sub> /C	Thermal treatment	1 M NaClO <sub>4</sub> in EC : PC (volume ratio 1 : 1) with 5% FEC	282 mAhg <sup>-1</sup> after 300 cycles at 0.05 C	413 mAhg <sup>-1</sup> at 10 C	68.9%	[111]
Bi <sub>2</sub> S <sub>3</sub> /rGO	hydrothermal	1 M NaCF <sub>3</sub> SO <sub>3</sub> in DEGDME	120.3 mAhg <sup>-1</sup> after 3400 cycles at 10 Ag <sup>-1</sup>	237.5 mAhg <sup>-1</sup> at 15 Ag <sup>-1</sup>	97.43%	[133]
Bi <sub>2</sub> S <sub>3</sub> xSe <sub>y</sub> @rGO	Solvothermal	N/A	721.6 mAhg <sup>-1</sup> after 100 cycles at 0.1 Ag <sup>-1</sup>	613.1 mAhg <sup>-1</sup> at 2 Ag <sup>-1</sup>	About 90%	[134]

Material	Synthesis method	Electrolyte	Cycle performance	Rate performance	ICE	Ref
2D-Bi <sub>2</sub> Se <sub>3</sub>	Solvothermal	N/A	370 mAh g <sup>-1</sup> after 500 cycles at 5 A g <sup>-1</sup>	250 mAh g <sup>-1</sup> at 10 A g <sup>-1</sup>	About 80%	[116]
Bi <sub>2</sub> O <sub>2</sub> Se/Bi <sub>4</sub> Se <sub>3</sub> @CNTs@GO	Thermal treatment	1 M NaCF <sub>3</sub> SO <sub>3</sub> in DIGLYME	102 mAh g <sup>-1</sup> after 1000 cycles at 1 A g <sup>-1</sup>	80 mAh g <sup>-1</sup> at 5 A g <sup>-1</sup>	98.1%	[135]
G-Bi <sub>2</sub> Se <sub>3</sub> /C	CVD	1 M NaClO <sub>4</sub> in EC : DMC (volume ratio 1:1) with 5% FEC	160.1 mAh g <sup>-1</sup> after 300 cycles at 0.05 A g <sup>-1</sup>	119.9 mAh g <sup>-1</sup> at 5 A g <sup>-1</sup>	49.1%	[51]
Bi <sub>2</sub> Se <sub>3</sub> /MXene/SWCNT	Solution method	1 M NaClO <sub>4</sub> in PC with 5% FEC	375 mAh g <sup>-1</sup> after 100 cycles at 0.1 A g <sup>-1</sup>	286.3 mAh g <sup>-1</sup> at 5 A g <sup>-1</sup>	90.7%	[49]
s-Bi <sub>2</sub> Se <sub>3</sub>	Solvothermal	1 M NaPF <sub>6</sub> in DME	247 mAh g <sup>-1</sup> after 100 cycles at 0.1 A g <sup>-1</sup>	231 mAh g <sup>-1</sup> at 5 A g <sup>-1</sup>	N/A	[58]
Bi <sub>2</sub> Se <sub>3</sub> -Se <sub>x</sub> @ReS <sub>2</sub>	Solvothermal	1 M NaPF <sub>6</sub> in DIGLYME	426.9 mAh g <sup>-1</sup> after 100 cycles at 0.5 A g <sup>-1</sup>	365 mAh g <sup>-1</sup> at 30 A g <sup>-1</sup>	64.2%	[120]

systems. However, it is crucial to acknowledge that ether-based electrolytes are not suitable for high operating voltages. Therefore, cathodes with operating voltages below 4 V are preferred, particularly polyanion-type cathodes, which provide both high energy density and excellent stability.

## Acknowledgements

This work was supported by the National Natural Science Foundation of China (No. 52101267, U23A20122), Liaoning Provincial Science and Technology Plan Joint Plan (Applied Basic Research Project, 2023JH2/101700274), and Scientific Research Project of the Liaoning Provincial Education Department (No. LJ222410142037).

## Conflict of Interests

The authors declare no conflict of interest.

**Keywords:** Sodium ion batteries • Bismuth • Structure regulation • Volume expansion • Surface engineering

- [1] K. Chayambuka, G. Mulder, D. L. Danilov, P. H. L. Notten, *Adv. Energy Mater.* **2020**, *10*, 2001310.
- [2] Z. Guo, G. Qian, C. Wang, G. Zhang, R. Yin, W.-D. Liu, R. Liu, Y. Chen, *Prog. Nat. Sci.-Mater. Int.* **2023**, *33*, 1–7.
- [3] J.-Y. Hwang, S.-T. Myung, Y.-K. Sun, *Chem. Soc. Rev.* **2017**, *46*, 3529–3614.
- [4] M. Sawicki, L. L. Shaw, *RSC Adv.* **2015**, *5*, 53129–53154.
- [5] Z. Tian, Y. Zou, G. Liu, Y. Wang, J. Yin, J. Ming, H. N. Alshareef, *Adv. Sci. (Weinh.)* **2022**, *9*, 2201207.
- [6] J. Kim, Y. Kim, J. Yoo, G. Kwon, Y. Ko, K. Kang, *Nat. Rev. Mater.* **2023**, *8*, 54–70.
- [7] Z. Li, J. Tan, C. Gao, Y. Wang, Y. Wang, M. Ye, J. Shen, *Energy Environ. Sci.* **2023**, *16*, 2398–2431.
- [8] S. Qiao, Q. Zhou, M. Ma, H. K. Liu, S. X. Dou, S. Chong, *ACS Nano* **2023**, *17*, 11220–11252.
- [9] P. Xiao, X. Yun, Y. Chen, X. Guo, P. Gao, G. Zhou, C. Zheng, *Chem. Soc. Rev.* **2023**, *52*, 5255–5316.
- [10] Z. Zhu, T. Jiang, M. Ali, Y. Meng, Y. Jin, Y. Cui, W. Chen, *Chem. Rev.* **2022**, *122*, 16610–16751.
- [11] Y. Chu, J. Zhang, Y. Zhang, Q. Li, Y. Jia, X. Dong, J. Xiao, Y. Tao, Q.-H. Yang, *Adv. Mater.* **2023**, *35*, 2212186.
- [12] H. Gao, J. Li, F. Zhang, C. Li, J. Xiao, X. Nie, G. Zhang, Y. Xiao, D. Zhang, X. Guo, Y. Wang, Y.-M. Kang, G. Wang, H. Liu, *Adv. Energy Mater.* **2024**, *14*, 2304529.
- [13] Z. Tang, S. Zhou, Y. Huang, H. Wang, R. Zhang, Q. Wang, D. Sun, Y. Tang, H. Wang, *Electrochim. Energy Rev.* **2023**, *6*, 8.
- [14] X. Chen, C. Liu, Y. Fang, X. Ai, F. Zhong, H. Yang, Y. Cao, *Carbon Energy* **2022**, *4*, 1133–1150.
- [15] Y. Lu, L. Yu, X. W. Lou, *Chem* **2018**, *4*, 972–996.
- [16] F. Wang, B. Wang, J. Li, B. Wang, Y. Zhou, D. Wang, H. Liu, S. Dou, *ACS Nano* **2021**, *15*, 2197–2218.
- [17] S.-H. Yu, S. H. Lee, D. J. Lee, Y.-E. Sung, T. Hyeon, *Small* **2016**, *12*, 2146–2172.
- [18] M. Lao, Y. Zhang, W. Luo, Q. Yan, W. Sun, S. X. Dou, *Adv. Mater.* **2017**, *29*, 1700622.
- [19] S. Liang, Y.-J. Cheng, J. Zhu, Y. Xia, P. Mueller-Buschbaum, *Small Methods* **2020**, *4*, 2000218.
- [20] Q. Man, Y. An, C. Liu, H. Shen, S. Xiong, J. Feng, *J. Energy Chem.* **2023**, *76*, 576–600.
- [21] M. Peng, K. Shin, L. Jiang, Y. Jin, K. Zeng, X. Zhou, Y. Tang, *Angew. Chem. Int. Ed.* **2022**, *61*, e202206770.

- [22] K. Song, C. Liu, L. Mi, S. Chou, W. Chen, C. Shen, *Small* **2021**, *17*, 1903194.
- [23] X. Cheng, D. Li, Y. Jiang, F. Huang, S. Li, *Coatings* **2023**, *13*, 2088.
- [24] X. Cheng, D. Li, Y. Jiang, F. Huang, S. Li, *Materials (Basel)* **2024**, *17*, 21.
- [25] Y. Feng, Y. Lv, H. Fu, M. Parekh, A. M. Rao, H. Wang, X. Tai, X. Yi, Y. Lin, J. Zhou, B. Lu, *Nat. Sci. Rev.* **2023**, *10*, nwad118.
- [26] J. H. Jia, X. F. Lu, C. C. Yang, Q. Jiang, *J. Mater. Chem. A* **2024**, *12*, 1359–1391.
- [27] Y. Wang, X. Xu, F. Li, S. Ji, J. Zhao, J. Liu, Y. Huo, *Batter.-Basel* **2023**, *9*, 440.
- [28] X. Zhou, X. Chen, W. Kuang, X. Zhang, X. Wu, X. Chen, C. Zhang, L. Li, S.-L. Chou, *Chem Sci* **2024**, *15*, 12189–12199.
- [29] Y. H. Kim, J. H. An, S. Y. Kim, X. Li, E. J. Song, J. H. Park, K. Y. Chung, Y. S. Choi, D. O. Scanlon, H. J. Ahn, J. C. Lee, *Adv. Mater.* **2022**, *34*, 2201446.
- [30] J. Zhou, Y. Ding, Y. Wang, H. Li, J. Shang, Y. Cao, H. Wang, *J. Colloid Interface Sci.* **2024**, *657*, 502–510.
- [31] Z. Li, Y. Zhang, J. Zhang, Y. Cao, J. Chen, H. Liu, Y. Wang, *Angew. Chem. Int. Ed.* **2022**, *61*, e202116930.
- [32] X. Li, Y. Xing, G. Song, C. Qin, L. Xu, L. Huang, *Nano* **2022**, *17*, 2250006.
- [33] H. Long, J. Wang, S. Zhao, B. Zou, L. Yan, Q. Huang, Y. Zhao, *Angew. Chem. Int. Ed.* **2024**, *63*, e202406513.
- [34] P. Xiong, P. Bai, A. Li, B. Li, M. Cheng, Y. Chen, S. Huang, Q. Jiang, X. H. Bu, Y. Xu, *Adv. Mater.* **2019**, *31*, 1904771.
- [35] B. Liu, W. Yao, P. Qin, J. Qian, X. Ding, *J. Storage Mater.* **2024**, *89*, 111921.
- [36] L. Li, H. Jiang, N. Xu, X. Lian, H. Huang, H. Geng, S. Peng, *J. Mater. Chem. A* **2021**, *9*, 17336–17343.
- [37] H. Yin, Q. Li, M. Cao, W. Zhang, H. Zhao, C. Li, K. Huo, M. Zhu, *Nano Res.* **2017**, *10*, 2156–2167.
- [38] R. C. Cui, H. Y. Zhou, J. C. Li, C. C. Yang, Q. Jiang, *Adv. Funct. Mater.* **2021**, *31*, 2103067.
- [39] Y. Jin, H. Yuan, J.-L. Lan, Y. Yu, Y.-H. Lin, X. Yang, *Nanoscale* **2017**, *9*, 13298–13304.
- [40] H. Yin, M.-L. Cao, X.-X. Yu, H. Zhao, Y. Shen, C. Li, M.-Q. Zhu, *Mater. Chem. Front.* **2017**, *1*, 1615–1621.
- [41] Y. Liang, N. Song, Z. Zhang, W. Chen, J. Feng, B. Xi, S. Xiong, *Adv. Mater.* **2022**, *34*, 2202673.
- [42] K. H. Nam, V. Ganesan, D. H. Kim, J. H. Choi, C. M. Park, *Int. J. Energy Res.* **2022**, *46*, 9486–9497.
- [43] Y. Guo, G. Wang, B. Peng, J. Li, J. Ding, G. Zhang, *ACS Appl. Energy Mater.* **2021**, *4*, 8285–8293.
- [44] L. Chen, X. He, H. Chen, S. Huang, M. Wei, *J. Mater. Chem. A* **2021**, *9*, 22048–22055.
- [45] X. Zhang, X. Qiu, J. Lin, Z. Lin, S. Sun, J. Yin, H. N. Alshareef, W. Zhang, *Small* **2023**, *19*, 2302071.
- [46] Z.-H. Lin, X.-Q. Qiu, X.-H. Zu, X.-S. Zhang, L. Zhong, S.-R. Sun, S.-H. Hao, Y.-J. Sun, W.-L. Zhang, *Rare Met.* **2023**, *43*, 1037–1047.
- [47] W. Yang, H. Wang, T. Liu, L. Gao, *Mater. Lett.* **2016**, *167*, 102–105.
- [48] Z. Hu, X. Li, J. Qu, Z. Zhao, H. Xie, H. Yin, *J. Power Sources* **2021**, *496*, 229830.
- [49] B. He, J. Cunha, Z. Hou, G. Li, H. Yin, *J. Colloid Interface Sci.* **2023**, *650*, 857–864.
- [50] M. Wang, H. Li, X. Cheng, S. Tian, X. Wang, *Batter. Supercaps* **2023**, *6*, e202300055.
- [51] S. Chong, L. Yuan, S. Qiao, M. Ma, T. Li, X. L. Huang, Q. Zhou, Y. Wang, W. Huang, *Sci. China Mater.* **2023**, *66*, 2641–2651.
- [52] S. Qiao, Y. Liu, K. Wang, S. Chong, *Batteries* **2023**, *9*, 505.
- [53] H. Zhu, F. Wang, L. Peng, T. Qin, F. Kang, C. Yang, *Angew. Chem. Int. Ed.* **2022**, *62*, e202212439.
- [54] H. Ma, J. Li, J. Yang, N. Wang, Z. Liu, T. Wang, D. Su, C. Wang, G. Wang, *Chem. – An Asian J.* **2021**, *16*, 3774–3780.
- [55] H. Zhang, R. Khan, Y. Chen, J. Zhu, L. Huang, Y. Wu, *ACS Appl. Energy Mater.* **2022**, *5*, 13452–13460.
- [56] Y. Gogotsi, B. Anasori, *ACS Nano* **2019**, *13*, 8491–8494.
- [57] Q. Yang, W. Gao, W. Zhong, M. Tao, Y. Qi, S.-J. Bao, M. Xu, *New J. Chem.* **2020**, *44*, 3072–3077.
- [58] R. Meija, V. Lazarenko, Y. Rublova, A. Kons, V. Voikiva, J. Andzane, O. Gogotsi, I. Baginskis, V. Zahorodna, A. Sarakovskis, A. Pludons, A. Sutka, A. Viksna, D. Erts, *Sustain. Mater. Technol.* **2023**, *38*, e00768.
- [59] J. Yang, Y. Wang, W. Li, L. Wang, Y. Fan, W. Jiang, W. Luo, Y. Wang, B. Kong, C. Selomulya, H. K. Liu, S. X. Dou, D. Zhao, *Adv. Mater.* **2017**, *29*, 1700523.
- [60] Y. Dong, M. Abbasi, J. Meng, L. German, C. Carlos, J. Li, Z. Zhang, D. Morgan, J. Hwang, X. Wang, *Nat. Commun.* **2023**, *14*, 1865.
- [61] Z. Li, Y. Zhang, K. Zhou, T. Kong, X. Zhou, Y. Hao, X. Huang, J. Xu, Y. Cheng, H. Liu, Z. Guo, Y. Wang, *Adv. Energy Mater.* **2024**, *14*, 2303786.
- [62] H. Yang, R. Xu, Y. Yao, S. Ye, X. Zhou, Y. Yu, *Adv. Funct. Mater.* **2019**, *29*, 1809195.
- [63] H. Yang, L.-W. Chen, F. He, J. Zhang, Y. Feng, L. Zhao, B. Wang, L. He, Q. Zhang, Y. Yu, *Nano Lett.* **2019**, *20*, 758–767.
- [64] B. Pu, Y. Liu, J. Bai, X. Chu, X. Zhou, Y. Qing, Y. Wang, M. Zhang, Q. Ma, Z. Xu, B. Zhou, W. Yang, *ACS Nano* **2022**, *16*, 18746–18756.
- [65] B. Park, S. Lee, D.-Y. Han, H. Jang, D. Gi Seong, J.-K. Yoo, S. Park, Y. Oh, J. Ryu, *Appl. Surf. Sci.* **2023**, *614*, 156188.
- [66] C. Shen, T. Cheng, C. Liu, L. Huang, M. Cao, G. Song, D. Wang, B. Lu, J. Wang, C. Qin, X. Huang, P. Peng, X. Li, Y. Wu, *J. Mater. Chem. A* **2020**, *8*, 453–460.
- [67] A. Xu, Q. Zhu, G. Li, C. Gong, X. Li, H. Chen, J. Cui, S. Wu, Z. Xu, Y. Yan, *Small* **2022**, *18*, 2203976.
- [68] Z. Chen, X. Wu, Z. Sun, J. Pan, J. Han, Y. Wang, H. Liu, Y. Shen, J. Li, D. L. Peng, Q. Zhang, *Adv. Energy Mater.* **2024**, *14*, 2400132.
- [69] X. Cheng, D. Li, Y. Wu, R. Xu, Y. Yu, *J. Mater. Chem. A* **2019**, *7*, 4913–4921.
- [70] F. Yang, F. Yu, Z. Zhang, K. Zhang, Y. Lai, J. Li, *Chem. – A Eur. J.* **2016**, *22*, 2333–2338.
- [71] J. Zhu, J. Wang, G. Li, L. Huang, M. Cao, Y. Wu, *J. Mater. Chem. A* **2020**, *8*, 25746–25755.
- [72] M. Z. Xu, S. Q. Gong, Y. L. Niu, K. Y. Zhang, T. Liu, Z. F. Chen, *Sci. China Mater.* **2023**, *66*, 106–117.
- [73] S. H. Qi, X. Xie, X. W. Peng, D. H. L. Ng, M. G. Wu, Q. H. Liu, J. L. Yang, J. M. Ma, *Phys. Status Solidi-RRL* **2019**, *13*, 1900209.
- [74] K. Zong, T. Z. Chu, D. Q. Liu, A. Mehmood, T. J. Fan, W. Raza, A. Hussain, Y. G. Deng, W. Liu, A. Saad, J. Zhao, Y. Li, D. Aurbach, X. K. Cai, *Small* **2022**, *18*, 2204236.
- [75] G. Z. Cheng, S. Liu, Y. X. Su, X. J. Wang, X. R. Li, J. Shi, M. H. Huang, Z. C. Shi, H. L. Wang, *J. Alloys Compd.* **2022**, *913*, 147450.
- [76] H. Yin, Q. W. Li, M. L. Cao, W. Zhang, H. Zhao, C. Li, K. F. Huo, M. Q. Zhu, *Nano Res.* **2017**, *10*, 2156–2167.
- [77] H. Long, X. Yin, X. Wang, Y. Zhao, L. Yan, *J. Energy Chem.* **2022**, *67*, 787–796.
- [78] S. Wei, W. Li, Z. Ma, X. Deng, Y. Li, X. Wang, *Small* **2023**, *19*, 2304265.
- [79] Z. Sun, Y. Liu, W. Ye, J. Zhang, Y. Wang, Y. Lin, L. Hou, M. S. Wang, C. Yuan, *Angew. Chem. Int. Ed.* **2021**, *60*, 7180–7187.
- [80] X. Chen, Y. Li, Y. Xu, J. Tang, Y. Yao, J. Hu, *Mater. Lett.* **2024**, *370*, 136819.
- [81] X. Cheng, R. Shao, D. Li, H. Yang, Y. Wu, B. Wang, C. Sun, Y. Jiang, Q. Zhang, Y. Yu, *Adv. Funct. Mater.* **2021**, *31*, 2011264.
- [82] J. Bai, Y. Liu, B. Pu, Q. Tang, Y. Wang, R. Yuan, J. Cui, Y. Yang, X. Zheng, B. Zhou, W. Yang, *J. Mater. Chem. A* **2024**, *12*, 11691–11700.
- [83] J. Qiu, S. Li, X. Su, Y. Wang, L. Xu, S. Yuan, H. Li, S. Zhang, *Chem. Eng. J.* **2017**, *320*, 300–307.
- [84] L. Wang, A. A. Voskanyan, K. Y. Chan, B. Qin, F. Li, *ACS Appl. Energy Mater.* **2019**, *3*, 565–572.
- [85] Y. Liang, N. Song, M. Zhang, X. An, K. Song, W. Chen, J. Feng, S. Xiong, B. Xi, *Adv. Energy Mater.* **2023**, *13*, 2302825.
- [86] H. Gao, J. Niu, C. Zhang, Z. Peng, Z. Zhang, *ACS Nano* **2018**, *12*, 3568–3577.
- [87] Y. Zhu, C. Wang, Z. Cheng, Q. Yao, J. Su, B. Chen, J. Yang, Y. Qian, *Chem. Commun.* **2022**, *58*, 5140–5143.
- [88] J. Ni, X. Li, M. Sun, Y. Yuan, T. Liu, L. Li, J. Lu, *ACS Nano* **2020**, *14*, 9117–9124.
- [89] M. Chen, X. Han, X. Zheng, H. Shen, J. Wang, J. You, L. Yan, X. Meng, Q. Kang, Q. Wu, Y. Zhao, T. Ma, *Electrochim. Acta* **2024**, *478*, 143867.
- [90] X. Han, X. Zheng, J. You, J. Wang, J. Hou, Z. Zhu, T. Ma, M. Chen, *Chem. Eng. J.* **2024**, *490*, 151975.
- [91] J. Zhao, J. Xu, Q. Li, W. Yao, C. Yu, N. Zhang, X. Chen, X. Ding, *J. Electroanal. Chem.* **2023**, *939*, 117452.
- [92] X. Wang, B. Feng, L. Huang, Q. Fu, W. Li, C. Zhu, P. Chen, C. Yang, Y.-L. Ding, *J. Power Sources* **2022**, *520*, 230826.
- [93] W. Zhang, W. Yan, H. Jiang, C. Wang, Y. Zhou, F. Ke, H. Cong, H. Deng, *ACS Sustain. Chem. Eng.* **2020**, *8*, 335–342.
- [94] R. Fu, J. Pan, M. Wang, H. Min, H. Dong, R. Cai, Z. Sun, Y. Xiong, F. Cui, S.-Y. Lei, S. Chen, J. Chen, L. Sun, Q. Zhang, F. Xu, *ACS Nano* **2023**, *17*, 12483–12498.
- [95] P. Xiong, J. Wu, M. Zhou, Y. Xu, *ACS Nano* **2019**, *14*, 1018–1026.
- [96] C. Huang, A. Xu, G. Li, H. Sun, S. Wu, Z. Xu, Y. Yan, *Small* **2021**, *17*, 2100685.
- [97] Y. Zhao, A. Manthiram, *Chem. Mater.* **2015**, *27*, 3096–3101.

- [98] X. Hou, Y. Zhu, Q. Yao, J. Song, C. Wang, Y. Zhou, S. Zeng, J. Yang, Y. Qian, *J. Energy Chem.* **2023**, *79*, 468–476.
- [99] H. Yang, L. Y. Yang, A. Abiliz, S. Y. Wang, F. J. Zhao, M. Zhang, J. Li, H. B. Li, *Ionicics* **2021**, *27*, 1429–1437.
- [100] L. Cheng, H. Liu, X. Tan, J. Zhang, J. Wei, H. Lv, J. Shi, X. Tang, *J. Phys. Chem. C* **2014**, *118*, 904–910.
- [101] J. Sun, M. Li, J. A. S. Oh, K. Zeng, L. Lu, *Mater. Technol.* **2018**, *33*, 563–573.
- [102] D. Su, S. Dou, G. Wang, *Nano Energy* **2015**, *12*, 88–95.
- [103] H. Gao, W. Ma, W. Yang, J. Wang, J. Niu, F. Luo, Z. Peng, Z. Zhang, *J. Power Sources* **2018**, *379*, 1–9.
- [104] Y. Huang, C. Zhu, S. Zhang, X. Hu, K. Zhang, W. Zhou, S. Guo, F. Xu, H. Zeng, *Nano Lett.* **2019**, *19*, 1118–1123.
- [105] J. Sottmann, M. Herrmann, P. Vajeeston, Y. Hu, A. Ruud, C. Drathen, H. Emerich, H. Fjellvåg, D. S. Wragg, *Chem. Mater.* **2016**, *28*, 2750–2756.
- [106] C. Nithya, *ChemPlusChem* **2015**, *80*, 1000–1006.
- [107] E. Demir, S. Hayat Soytas, R. Demir-Cakan, *Solid State Ion.* **2019**, *342*, 115066.
- [108] C. Xu, Y. Tian, J. Sun, M. Li, W. Song, J. You, M. Feng, X. Wang, P. Wang, H. Li, G. Zhang, Y. He, Z. Liu, *ACS Appl. Mater. Interfaces* **2023**, *15*, 1891–1902.
- [109] J. Ni, Y. Zhao, T. Liu, H. Zheng, L. Gao, C. Yan, L. Li, *Adv. Energy Mater.* **2014**, *4*, 1400798.
- [110] J. Ma, Z. Liu, J. Lian, X. Duan, T. Kim, P. Peng, X. Liu, Q. Chen, G. Yao, W. Zheng, *CrystEngComm* **2011**, *13*, 3072–3079.
- [111] H. Kim, D. Kim, Y. Lee, D. Byun, H.-S. Kim, W. Choi, *Chem. Eng. J.* **2020**, *383*, 123094.
- [112] D. Zhang, Y. Shao, J. Wang, Z. Li, Q. Wang, H. Sun, Q. Sun, B. Wang, *Small Struct.* **2023**, *5*, 2300217.
- [113] R. Cai, W. Zhang, J. Zhou, K. Yang, L. Sun, L. Yang, L. Ran, R. Shao, T. Fukuda, G. Tan, H. Liu, J. Wan, Q. Zhang, L. Dong, *Small Methods* **2022**, *6*, 2200995.
- [114] W. Sun, X. Rui, D. Zhang, Y. Jiang, Z. Sun, H. Liu, S. Dou, *J. Power Sources* **2016**, *309*, 135–140.
- [115] Y. Dong, M. Hu, Z. Zhang, J. A. Zapien, X. Wang, J.-M. Lee, *Nanoscale* **2018**, *10*, 13343–13350.
- [116] M. A. Ud Din, S. Irfan, S. Jamil, S. U. Dar, Q. U. Khan, M. S. Saleem, N. Cheng, *J. Alloys Compd.* **2022**, *901*, 163572.
- [117] W. Liang, B. Chen, W. Lin, L. Shao, X. Shi, Z. Sun, *Mater. Lett.* **2023**, *332*, 133542.
- [118] A. Wang, W. Hong, L. Li, R. Guo, Y. Xiang, Y. Ye, W. Deng, G. Zou, H. Hou, X. Ji, *Energy Storage Mater.* **2022**, *53*, 1–12.
- [119] D. Li, J. Hu, C. Wang, L. Guo, J. Zhou, *J. Power Sources* **2023**, *555*, 232387.
- [120] Z. Sun, M. Liu, R. Khan, L. Huang, Y. Wu, Y. Zhou, *Mater. Today Chem.* **2023**, *29*, 101401.
- [121] P. Liu, J. Han, K. Zhu, Z. Dong, L. Jiao, *Adv. Energy Mater.* **2020**, *10*, 2000741.
- [122] D. Sun, K. Liu, J. Hu, J. Zhou, *Small* **2021**, *17*, 2006374.
- [123] Y. Huang, X. Zhu, D. Cai, Z. Cui, Q. Wang, H. Zhan, *J. Energy Chem.* **2021**, *59*, 473–481.
- [124] X. Li, S. Xiao, D. Guo, J. Jiang, X. Niu, R. Wu, T. Pan, J. Song Chen, *Chem. Eng. J.* **2023**, *452*, 139363.
- [125] J. Wang, W. Bai, Y. Zhou, H. Zhou, Y. Cao, Z. Wang, Y. Zhang, W. Pan, *J. Storage Mater.* **2024**, *76*, 109743.
- [126] M. Han, Z. Zhou, Y. Li, Q. Chen, M. Chen, *J. Alloys Compd.* **2022**, *892*, 162143.
- [127] Z. Zhao, K. Li, C. Li, X. Pei, S. Zhang, Z. Liu, X. Du, D. Li, *ACS Appl. Mater. Interfaces* **2023**, *15*, 4011–4020.
- [128] M. Xie, C. Li, S. Zhang, Z. Zhang, Y. Li, X. B. Chen, Z. Shi, S. Feng, *Small* **2023**, *19*, 2301436.
- [129] R. Liu, L. Yu, X. He, H. Liu, X. Ma, Z. Tao, G. Wan, N. Ahmad, B. Peng, L. Shi, G. Zhang, *eScience* **2023**, *3*, 100138.
- [130] W. Luo, F. Li, Q. Li, X. Wang, W. Yang, L. Zhou, L. Mai, *ACS Appl. Mater. Interfaces* **2018**, *10*, 7201–7207.
- [131] Y. Li, M. Han, Z. Zhou, X. Xia, Q. Chen, M. Chen, *ChemElectroChem* **2021**, *8*, 697–704.
- [132] Y. Wang, X. Xu, Y. Wu, F. Li, W. Fan, Y. Wu, S. Ji, J. Zhao, J. Liu, Y. Huo, *Adv. Energy Mater.* **2024**, *14*, 2401833.
- [133] X. Sun, L. Wang, C. Li, D. Wang, I. Sikandar, R. Man, F. Tian, Y. Qian, L. Xu, *Nano Res.* **2021**, *14*, 4696–4703.
- [134] M. Han, Y. Xi, S. Luan, J. Zhou, F. Gao, *Mater. Chem. Phys.* **2022**, *292*.
- [135] H. Liu, D. Li, H. Liu, C. Wang, Y. Wang, Y. Chen, Y. Linghu, Z. Tian, H. Song, J. Zhou, L. Guo, *J. Colloid Interface Sci.* **2022**, *620*, 168–178.
- [136] J. Lin, S. Lu, Y. Zhang, L. Zeng, Y. Zhang, H. Fan, *J. Colloid Interface Sci.* **2023**, *645*, 654–662.

Manuscript received: August 31, 2024

Revised manuscript received: November 11, 2024

Accepted manuscript online: November 19, 2024

Version of record online: December 5, 2024